

2017

Computational Wave Field Modeling using Sequential Mapping of Poly-Crepitus Green's Function in Anisotropic Media

Sajan Shrestha
University of South Carolina - Columbia

Follow this and additional works at: <https://scholarcommons.sc.edu/etd>



Part of the [Mechanical Engineering Commons](#)

Recommended Citation

Shrestha, S.(2017). *Computational Wave Field Modeling using Sequential Mapping of Poly-Crepitus Green's Function in Anisotropic Media*. (Doctoral dissertation). Retrieved from <https://scholarcommons.sc.edu/etd/4419>

This Open Access Dissertation is brought to you by Scholar Commons. It has been accepted for inclusion in Theses and Dissertations by an authorized administrator of Scholar Commons. For more information, please contact digres@mailbox.sc.edu.

COMPUTATIONAL WAVE FIELD MODELING USING SEQUENTIAL
MAPPING OF POLY-CREPITUS GREEN'S FUNCTION IN
ANISOTROPIC MEDIA

by

Sajan Shrestha

Bachelor of Science
Benedict College, 2014

Submitted in Partial Fulfillment of the Requirements

For the Degree of Master of Science in

Mechanical Engineering

College of Engineering and Computing

University of South Carolina

2017

Accepted by:

Sourav Banerjee, Director of Thesis

Victor Giurgiutiu, Reader

Cheryl L. Addy, Vice Provost and Dean of the Graduate School

© Copyright by Sajan Shrestha, 2017
All Rights Reserved.

DEDICATION

This thesis work is dedicated to the author's parents: Ram Krishna Shrestha and Kalpana Shrestha and all his family members as well as his advisor, Sourav Banerjee.

ACKNOWLEDGEMENTS

The author would like to thank his advisor, Dr. Sourav Banerjee for his advice for author's improvement not just as a researcher but also, as an individual, He would also like to thank his lab colleagues for always providing fun and optimal environment in the lab for conducting the research. Finally, the author would like to acknowledge NASA Langley Research Center (LaRC) for funding the research under Contract number>NNL15AA16C.

ABSTRACT

In this thesis, a meshless semi-analytical computational method is presented to compute the ultrasonic wave field in the generalized anisotropic material while understanding the physics of wave propagation in detail. To understand the wave-damage interaction in an anisotropic material, it is neither feasible nor cost-effective to perform multiple experiments in the laboratory. Hence, recently the computational nondestructive evaluation (CNDE) received much attention to performing the NDE experiments in a virtual environment. In this thesis, a fundamental framework is constructed to perform the CNDE experiment of a thick composite specimen in a Pulse-Echo (PE) mode. To achieve the target, the following processes were proposed. The solution of the elastodynamic Green's function at a spatial point in an anisotropic media was first obtained by solving the fundamental elastodynamic equation using Radon transform and spectral resolution theorem. Next, the basic concepts of wave propagation behavior in a generalized material and the visualization of the anisotropic bulk wave modes were accomplished by solving the Christoffel's Equation in 3D. Moreover, the displacement and stress Green's functions in a generalized anisotropic material were calculated in the frequency domain. Frequency domain Green's functions were achieved by superposing the effect of propagating eigen wave modes that were obtained from the Christoffel's solution and integrated over the all possible directions of wave propagation by discretizing a sphere. A MATLAB code was developed to compute the displacement and stress Green's functions numerically. Further, the numerically calculated Green's functions were implemented and integrated with the

meshless Distributed Point Source Method (DPSM). DPSM technique was used to virtually simulate a PE NDE experiments of a half-space anisotropic material, inspected by a circular transducer immersed in the fluid. The ultrasonic wave fields were calculated using DPSM after applying the boundary conditions and solving the unknown source strengths. A method named sequential mapping of poly-crepus Green's function was introduced and executed along with discretization angle optimization for the time-efficient computation of the wave fields. The full displacements and stress wave fields in transversely isotropic, fully orthotropic and monoclinic materials are presented in this thesis on different planes of the material.

TABLE OF CONTENTS

Dedication	iii
Acknowledgements	iv
Abstract.....	v
List of Figures.....	viii
List of Symbols	xi
List of Abbreviations.....	xiii
Chapter 1 Introduction.....	1
Chapter 2 Historical Background of Wave Field Modeling.....	5
Chapter 3 Concept of Anisotropy.....	9
Chapter 4 Waves in Anisotropic Media	13
Chapter 5 Numerical Computation of Green's Function	38
Chapter 6 Numerical Computation of Wave Field with the implementation of DPSM ..	44
Chapter 7 Conclusion and Future Endeavors	60
References	62
Appendix A: Anisogreen.m.....	68

LIST OF FIGURES

Figure 4.1 An artistic view showing the schematics of the wave field inside a bulk anisotropic media	13
Figure 4.2 a) Schematics of the wave surfaces and their relation b) relation of the phase velocity with the fundamental wave modes in anisotropic media.	16
Figure 4.3 Pictorial representation of the Christoffel's solution.....	20
Figure 4.4 For Aluminum: 3D Slowness plot, X-Y Contour plot, Y-Z Contour plot, and X-Z Contour plot of q_L , q_{S1} , q_{S2} modes	25
Figure 4.5 For Transversely Isotropic: 3D Slowness plot, X-Y Contour plot, Y-Z Contour plot, and X-Z Contour plot of q_L , q_{S1} , q_{S2} modes	26
Figure 4.6 For Orthotropic: 3D Slowness plot, X-Y Contour plot, Y-Z Contour plot, and X-Z Contour plot of q_L , q_{S1} , q_{S2} modes.....	27
Figure 4.7 For Monoclinic: 3D Slowness plot, X-Y Contour plot, Y-Z Contour plot, and X-Z Contour plot of q_L , q_{S1} , q_{S2} modes.....	28
Figure 4.8 A schematic diagram to visualize the Radon transform in 2D and 3D	31
Figure 4.9 A schematic diagram to visualize the displacement Green's function.....	36
Figure 5.1 Schematics of configurations to calculate the Green's function	39
Figure 5.2 Numerical computation of displacement Green's function due to forces acting along 1, 2 & 3directions when the inside material is Isotropic.....	39
Figure 5.3 Numerical computation of displacement Green's function due to forces acting along 1, 2 & 3directions when the inside material is Transversely Isotropic.	40
Figure 5.4 Numerical computation of displacement Green's function due to forces acting along 1, 2 & 3directions when the inside material is Orthotropic.	40
Figure 5.5 Numerical computation of displacement Green's function due to forces acting along 1, 2 & 3directions when the inside material is Monoclinic.	41

Figure 5.6 Numerical computation of displacement Green's function (unit mm) in Transversely Isotropic material.....	42
Figure 5.7 Numerical computation of Stress Green's function in Transversely Isotropic material due to source actuating along 1-direction	43
Figure 5.8 Numerical computation of Stress Green's function in Transversely Isotropic material due to source actuating along 3-direction	43
Figure 6.1 a) the total field at A is calculated by superposing the contribution of all point sources distributed along the boundary of the anisotropic medium. b) the three mutually perpendicular forces that are contained in the point source.....	45
Figure 6.2 a) Schematics (not to scale) of the wave field computation problem in anisotropic solid half space, point sources distributed over the x-y plane, however, only two orthogonal line of point sources are shown b) cross-section view of the NDE problem along x-z plane.....	46
Figure 6.3 A schematics showing the sequential mapping of Green's function, a) source and target point combinations b) extended target points in 2D c) Calculated Green's function on extended point sources d) Assignment of Green's function for an edge source e) source-target combinations in 3D, f) sequential mapping of 3D Green's function.....	53
Figure 6.4 a) Convergence study with the discretization angle for Green's function computation b) Increase in computational efficiency while solving a virtual NDE problem described in Fig. 2 in a transversely isotropic medium.....	54
Figure 6.5 Pressure and normal stress (σ_{33}) distribution at the fluid-solid interface	55
Figure 6.6 Wavefield plot a) Stress11 (σ_{11}) distribution in transversely isotropic half-space b) Stress33 (σ_{33}) distribution in transversely isotropic half-space in GPa.....	56
Figure 6.7 Wavefield plot a) Stress11 (σ_{11}) distribution in isotropic half-space b) Stress33 (σ_{33}) distribution in isotropic half space in GPa	56
Figure 6.8 Wavefield plot on x-z plane a) Stress11 (σ_{11}) distribution in fully orthotropic half-space b) Stress33 (σ_{33}) distribution in fully orthotropic half space in GPa	57
Figure 6.9 Wavefield plot on y-z plane a) Stress11 (σ_{11}) distribution in fully orthotropic half-space b) Stress33 (σ_{33}) distribution in fully orthotropic half space in GPa	58
Figure 6.10 Wavefield plot on x-z plane a) Stress11 (σ_{11}) distribution in monoclinic half space b) Stress33 (σ_{33}) distribution in monoclinic half space in GPa	58
Figure 6.11 Wavefield plot on y-z plane a) Stress11 (σ_{11}) distribution in monoclinic half space b) Stress33 (σ_{33}) distribution in monoclinic half space in GPa	59

LIST OF SYMBOLS

k	Vector representing the wave propagation direction
C_E	Velocity of the wave energy
φ	Skew Angle
C_P	Phase velocity
N	Wave energy propagation direction
n	Normal to the slowness surface
qL	Quasi Longitudinal Wave Mode
qSS	Quasi Shear Slow Wave Mode
$qS1$	Quasi Shear 1 Wave Mode
qFS	Quasi Shear Fast Wave Mode
$qS2$	Quasi Shear 2 Wave Mode
x_i	Components of vectors in the three Cartesian coordinates
σ_{ij}	The stress tensor
u_i	Displacement vector at a point in the solid
f_i	Body force per unit volume
C_{ijml}	Constitutive material property matrix
ε_{ml}	Strain tensor
A	Scalar amplitude of the wave
g_m	Polarization direction

ω	Monochromatic wave frequency
δ_{im}	Dirac delta function
ρ	Density of the material
C_{qL}	Phase Velocity for quasi longitudinal mode
C_{qFS}	Phase Velocity for quasi shear fast mode
C_{qSS}	Phase Velocity for quasi shear slow mode
$\boldsymbol{\varphi}_L$	Eigen vector for quasi longitudinal mode
$\boldsymbol{\varphi}_{FS}$	Eigen vector for quasi shear fast mode
$\boldsymbol{\varphi}_{SS}$	Eigen vector for quasi shear slow mode
G_{mp}	Time domain displacement Green's function
F_p	Force Amplitude
\mathcal{F}	Fourier transform
\tilde{G}_{mp}	Frequency-wavenumber domain displacement Green's function
\mathbf{L}_{im}	\mathcal{L}^2 Hilbert space operator
g_{mp}	Frequency domain displacement Green's function
C_{ij}	Reduced property matrix
R	Radon transform
h	Distance from the origin
$\vec{\hat{\mathbf{u}}}$	Unit Normal to the local orientation of lines
γ_z	z-th eigen value
P_{im}	Projection matrix of the eigen mode
H_z	Heaviside step function
θ	Spherical angle in spherical coordinate system
ϕ	Spherical angle in spherical coordinate system
s_z	Slowness Vector

LIST OF ABBREVIATIONS

BEM.....	Boundary Element Method
CST	Charge Simulation Technique
DPSM.....	Distributed Point Source Method
EFIT	Elastodynamic Finite Integration Technique
FEM	Finite Element Method
G-DPSM	Gaussian Distributed Point Source Method
IBIE.....	Indirect Boundary Integral Equation
M-GBM.....	Multi Gaussian Beam Model
MMP	Multiple Multi-Pole method
NDE	Non-Destructive Evaluation
SEM	Spectral Element Method
SHM.....	Structure Health Monitoring

CHAPTER 1

INTRODUCTION

With the advancement of human civilization, there has been a rapid evolution in the field of civil, mechanical and aerospace industry with the development of infrastructure such as highways, vehicles, aircrafts, etc. However, with the passage of time, the failure of these developed infrastructures is imminent. This inevitable failure of these structures can lead to economic harm, ecological imbalance, and loss of human lives. Hence, the scientists and engineers have researched to find different techniques such that it enables them to understand the state of the materials in these structures and risk factor involved with them. Nondestructive Evaluation (NDE) (Handbook 2009 April 7) is one such popular technique used for diagnosis of the structures, i.e., structural health monitoring (SHM) (Giurgiutiu 2014). NDE/SHM provides the understanding of the physics of the material interaction, characterization of the state of the material and the estimation of remaining useful life of the structure. Although many NDE techniques have been developed and used by researchers, the ultrasonic NDE (Sachse, Castagnede et al. 1990) is the most popular due to its capability to see the materials from the inside. A detailed study of ultrasonic wave propagation in different structures is essential for the optimal understanding of the ultrasonic nondestructive evaluation. The fundamental notion of ultrasonic nondestructive testing is to investigate the received ultrasonic signals to acquire information about the structures. The ultrasonic waves are introduced into the material with the help of ultrasonic or piezoelectric transducer as a probing energy, and the diagnosis of the material is carried

out by sensing the propagated energy from a distant location. For this purpose, there is an absolute need to understand the wave propagation behavior in these structures.

Understanding the wave propagation behavior in different types of materials, isotropic and anisotropic, has been a topic of interest and research since past few decades. Although the fluid and isotropic media is more or less saturated field, the critical wave propagation features in anisotropic media are still not fully understood. Due to the widespread application of engineered anisotropic materials, most popularly as composites, in many different areas of science and technology, significantly mechanical and aerospace industries, understanding the wave phenomena in these materials is of great importance. Wave propagation behavior is studied by investigating wave interaction with the material which manifests in the forms of reflection and transmission wave, giving rise to geometric dispersion. These interactions depend on many factors such as the geometric arrangements, mechanical properties, number and nature of the interfacial conditions and the loading conditions (Nayfeh 1995). The mechanical properties vary from the simple case of isotropic materials to the most general anisotropic ones, namely the "triclinic materials".

Using the ultrasonic NDE experiments, researchers have been able to quantify and understand the rudimentary damage states in the materials. However, the complex damaged states such as hidden delamination, kissing bonds, trapped cracks present in these materials are not visualized and understood appropriately. With the traditional NDE techniques, detecting such complex damages and understanding the ultrasonic wave signals due to the effect of those damages can be an overwhelming task. Waves in anisotropic media with complicated geometries are difficult to understand using the traditional ray tracing methods (Sachse, Castagnede et al. 1990, Pradhan, Venu Kumar et al. 1999, Moser, Weber et al.

2005). Moreover, it is neither feasible nor cost-effective to perform all the possible experiments with various damage scenarios (Mal, Yin et al. 1991, Mouchtachi, El Guerjouma et al. 2004, Moser, Weber et al. 2005, Li, Liu et al. 2013, Marguères and Meraghni 2013) and geometries. Hence, it is not possible to understand the ultrasonic wave interactions in the structure with all possible damages and material degradation with experiments. Consequently, such task can only be possible by correctly understanding the physics of waves propagation in anisotropic media and numerically simulating the behavior of the application of an accurate and efficient technique. The most effective way to do so is by developing a reliable technology capable of virtually simulating any NDE experiments in a systematic and computationally swift manner, i.e., computational NDE or virtual NDE.

The field of computational NDE or virtual NDE has been developing rapidly due to the necessity of simulating the elastodynamic wave phenomena in various materials in the most cost-effective and least computationally taxing fashion. Wave simulation is a theoretical field of research that began with the development of computer technology and numerical algorithms for solving differential and integral equations of several variables (Carcione 2007). In the field of computational wave modeling, these algorithms are important tools providing comprehension of wave propagation for a variety of applications. With the help of computational NDE, the researchers can compute the wave field for different materials with numerous wave-damage interaction scenarios and study the wave interaction behavior for those various situations. The knowledge gained in doing so can be schooled to identify and understand the quantitative fluctuation signals, which in turn will help us in the reliable interpretation of the real-life damage scenarios with the ability to

quantify the material properties. Moreover, some of these damages scenarios are, but not limited to, extent of internal damage and degree of material degradation (Sachse, Castagnede et al. 1990, Sahay, Kline et al. 1992, Hood and Mignogna 1995, Every and Kim 1996, Pradhan, Venu Kumar et al. 1999, Sharma 2002, Mouchtachi, El Guerjouma et al. 2004). To accomplish our ultimate goal of precise and prompt numerical wavefield modeling in any anisotropic structures with any complex scenarios, novel methodology and computational resources has to be optimally nominated. Hence, this thesis acts as a gateway to computational anisotropic wavefield modeling.

CHAPTER 2

HISTORICAL BACKGROUND OF WAVE FIELD MODELING

Studies of the elastic waves propagation in anisotropic media have been of great interest to researchers in the field of NDE. This interest is further intensified by the recent expansion in the use of anisotropic materials in the form of composite materials, super alloys, and crystal structures in the wide variety of applications. However, the inevitability of the necessity of NDE started during the World War II to realize the upsurge in demand for quality assurance of the mechanical systems, machine components and the defense equipment. With the end of the war, the focus of NDE industry shifted from the defense sector to the human infrastructures due to the colossal growth of industrial sectors. Also, the quality assurance of the aerospace systems such as airplanes, satellites, and spaceships became the new agenda for the government agencies.

In the post-war era, NDE was taken to further new heights with the invention and formulation of the novel configurations of the ultrasonic transducers for various applications. Hence, for the appropriate understanding of the ultrasonic wave field generated in front of the transducers and precise diagnosis of the state of the materials, it became essential to efficiently design the transducers as well as accurately interpret those ultrasonic signals. Even though the wave propagation behavior in the wires, rods, plates and various simpler structural components had been studied and understood, so was not the case for the ultrasonic transducers. Hence, the need has arisen for the understanding of the wave interaction phenomena in finite dimension transducers as it was different from

the application of plane wave assumption and the plane wave interaction for the structural components.

Moreover, this rising necessity resulted in the mathematical modeling of the ultrasonic wave using Rayleigh-Sommerfeld integral technique. The technique is simply known as the ray tracing method. The ray tracing method simplified the ultrasonic wave problem by representing the waves as rays. The mathematical analysis involves studying the incident waves and providing the reliable and intuitive understanding of the wave energy through the structure. This technique relies on the high-frequency assumption of the ray theory. With the evolution of the technique, it was later known as dynamic ray tracing technique which required the solution of the Eikonal equation (Biondi 1992) and was used in ultrasonic wave field modeling generated by the ultrasonic transducer. Dynamic ray tracing is an improvement over the previously proposed models with a paraxial approximation for the plane wave incidents. Since it is known that the incident wavefronts are neither plane nor spherical in the real experiments using transducers, we had an understanding which was inaccurate, therefore, incomplete. Also, the technique involved significant information loss due to failure to extract exact amplitude information and track all the wave modes in the complex media.

Similarly, about the development of the mathematical model of the anisotropic wave, the differences between wave propagation characteristics of isotropic and anisotropic media was first identified with the widely used bulk wave techniques. Later, Green's function solution, used in the formulation of integral representations and boundary integral equations for scattering problems and understanding of the elastodynamic response of an unbounded homogeneous linearly elastic solid, was used in modeling the wave in

anisotropic media(Achenbach 1975). Various techniques have been used in the derivation of Green's function. It has been derived using Cagniard de Hoop method by Kraut (Kraut 1963) for transversely isotropic half-space and by Burridge (Burridge 1971) for an anisotropic halfspace. Simplified method to Cagniard de Hoop has been used by Willis (Willis 1973, Willis 1991) and Payton (Payton 2012) for several anisotropic halfspace problems. The Green's function for unbounded, anisotropic elastic medium has been developed by Yeatts (Yeatts 1984). Moreover, the method has been further developed by Wang and Achenbach (Wang and Achenbach 1992, Wang and Achenbach 1993) to develop 2-D and 3-D Green's functions for anisotropic solids.

However, there remained the problem of inaccuracy in the modeling of both ultrasonic as well as anisotropic waves. To enhance the accuracy of modeling, various computational techniques have been developed and utilized by researchers, along with the advancement of technologies in past decades. Some of the popular computational simulation techniques used in the virtual NDE experiments are Finite Element Method (FEM) (Software 2009), Boundary Element Method (BEM) (Shaw 1979, X. Zhao. 2003), Indirect Boundary Integral Equation (IBIE) (M 1991, M 1993, Pointer T 1998, J 2007), Multi-Gaussian Beam Model (M-GBM) (J. J. Wen 1988, B. P. Newberry 1989, Spies 1999), Charge Simulation Technique (CST) (C. Rajamohan 1999), Multiple Multi-Pole method (MMP) (Ballisti 1983, Hafner 1985, Imhof 2004), Spectral Element Method (SEM) (J Moll 2011), Elastodynamic Finite Integration Technique (EFIT) (Cara A.C. Leckey 2014), Distributed Point Source Method (DPSM) (Placko and Kundu 2001, Placko, Kundu et al. 2002, Banerjee 2006, Banerjee and Kundu 2006, Banerjee 2007, Banerjee 2007, Banerjee and Kundu 2007, Placko and Kundu 2007, Banerjee 2008, Banerjee 2008,

Banerjee 2009), Gaussian Distributed Point Source Method (G-DPSM) (Rahani 2011) etc. Among all the techniques mentioned, FEM is the most dominant conventional method due to the availability of many commercial packages to perform these simulations. Unfortunately, spurious reflection at the element boundaries makes the FEM simulations incorrect. Moreover, it has also been found to be less accurate at higher frequencies. All competitive methods have their pros and cons. Hence, taking both the benefits and shortcomings into account, DPSM technique has been discussed and utilized in this thesis work to simulate the virtual NDE experiments. Nevertheless, before we proceed any further into the details of the DPSM, as pre-requisite we first briefly discuss the mechanics of anisotropic material and wave phenomena in an anisotropic material.

CHAPTER 3

CONCEPTS OF ANISOTROPY

Anisotropic materials have existed in the surrounding environment in nature. Some of the well-known natural anisotropic materials that we see in our daily lives are wood and stones which have been utilized to elevate our standard of living. Hence, due to its usefulness, anisotropic materials are also being engineered most famously as composites. In recent years, manufacturing and usage of composite materials in engineering field has skyrocketed as these materials can be engineered to a required specification. Anisotropic materials such as composites are a combination of two or more materials on a macroscopic scale to form an entirely new useful material. The well-designed composite material has improved properties such as strength stiffness, fatigue life, weight, acoustical insulation and so on.

3.1 Stress-Strain relations for Elastic Materials

The constitutive equation or generalized Hooke's law relating stresses and strains in anisotropic materials can be formulated in contracted notation as follows,

$$\sigma_i = C_{ij}\varepsilon_j$$

Where σ_i are the stress components in a (x, y, z) or (1, 2, 3) coordinate system, C_{ij} is the stiffness or material property matrix, ε_j are the strain components, and $i, j = 1, 2, \dots, 6$.

3.1.1 Stress-Strain relations for Anisotropic Materials

There are materials with the different complexity of anisotropy. Based on the complexity, these materials are categorized as triclinic being fully anisotropic, monoclinic, orthotropic, transversely isotropic and finally, an isotropic material with no anisotropy.

3.1.1.1 Triclinic Materials

The stiffness matrix, C_{ij} has 36 constants. However due to symmetry, there are only 21 independent constants. Therefore, the most general expression of constitutive equation for an elastic material is as follows.

$$\begin{bmatrix} \sigma_1 \\ \sigma_2 \\ \sigma_3 \\ \sigma_4 \\ \sigma_5 \\ \sigma_6 \end{bmatrix} = \begin{bmatrix} C_{11} & C_{12} & C_{13} & C_{14} & C_{15} & C_{16} \\ C_{12} & C_{22} & C_{23} & C_{24} & C_{25} & C_{26} \\ C_{13} & C_{23} & C_{33} & C_{34} & C_{35} & C_{36} \\ C_{14} & C_{24} & C_{34} & C_{44} & C_{45} & C_{46} \\ C_{15} & C_{25} & C_{35} & C_{45} & C_{55} & C_{56} \\ C_{16} & C_{26} & C_{36} & C_{46} & C_{56} & C_{66} \end{bmatrix} \begin{bmatrix} \varepsilon_1 \\ \varepsilon_2 \\ \varepsilon_3 \\ \varepsilon_4 \\ \varepsilon_5 \\ \varepsilon_6 \end{bmatrix}$$

The above relation characterizes the most general anisotropic material also known as triclinic material. The triclinic material has no planes of material symmetry, and the three material axes are oblique to one another.

3.1.1.2 Monoclinic Materials

Let's assume; there is one plane of material property symmetry, i.e., 1-2 plane or ($z = 0$) plane, then the constitutive equation reduces to

$$\begin{bmatrix} \sigma_1 \\ \sigma_2 \\ \sigma_3 \\ \sigma_4 \\ \sigma_5 \\ \sigma_6 \end{bmatrix} = \begin{bmatrix} C_{11} & C_{12} & C_{13} & 0 & 0 & C_{16} \\ C_{12} & C_{22} & C_{23} & 0 & 0 & C_{26} \\ C_{13} & C_{23} & C_{33} & 0 & 0 & C_{36} \\ 0 & 0 & 0 & C_{44} & C_{45} & 0 \\ 0 & 0 & 0 & C_{46} & C_{55} & 0 \\ C_{16} & C_{26} & C_{36} & 0 & 0 & C_{66} \end{bmatrix} \begin{bmatrix} \varepsilon_1 \\ \varepsilon_2 \\ \varepsilon_3 \\ \varepsilon_4 \\ \varepsilon_5 \\ \varepsilon_6 \end{bmatrix}$$

The above relation characterizes the anisotropic material known as monoclinic material.

The monoclinic material has one plane of material symmetry and has 13 independent elastic constants.

3.1.1.3 Orthotropic Materials

Similarly, if there are two planes of material property symmetry, then there will exist a third mutually orthogonal place with symmetry. Therefore, for the material with three mutually orthogonal planes of symmetry, the constitutive equation reduces to

$$\begin{bmatrix} \sigma_1 \\ \sigma_2 \\ \sigma_3 \\ \sigma_4 \\ \sigma_5 \\ \sigma_6 \end{bmatrix} = \begin{bmatrix} C_{11} & C_{12} & C_{13} & 0 & 0 & 0 \\ C_{12} & C_{22} & C_{23} & 0 & 0 & 0 \\ C_{13} & C_{23} & C_{33} & 0 & 0 & 0 \\ 0 & 0 & 0 & C_{44} & 0 & 0 \\ 0 & 0 & 0 & 0 & C_{55} & 0 \\ 0 & 0 & 0 & 0 & 0 & C_{66} \end{bmatrix} \begin{bmatrix} \varepsilon_1 \\ \varepsilon_2 \\ \varepsilon_3 \\ \varepsilon_4 \\ \varepsilon_5 \\ \varepsilon_6 \end{bmatrix}$$

The above relation characterizes the anisotropic material known as an orthotropic material.

The orthotropic material has three planes of material symmetry and has nine independent elastic constants. Also, there is no dependency between normal stress and shear strains as well as between shear stress and normal strains.

3.1.1.4 Transversely Isotropic Materials

Now, on top of the three mutually orthogonal planes of symmetry, if there exists a plane of isotropy, i.e., the material properties are same in all directions in that plane (let's assume 1-2 plane of isotropy), the constitutive equation reduces to

$$\begin{bmatrix} \sigma_1 \\ \sigma_2 \\ \sigma_3 \\ \sigma_4 \\ \sigma_5 \\ \sigma_6 \end{bmatrix} = \begin{bmatrix} C_{11} & C_{12} & C_{13} & 0 & 0 & 0 \\ C_{12} & C_{11} & C_{13} & 0 & 0 & 0 \\ C_{13} & C_{13} & C_{33} & 0 & 0 & 0 \\ 0 & 0 & 0 & C_{44} & 0 & 0 \\ 0 & 0 & 0 & 0 & C_{44} & 0 \\ 0 & 0 & 0 & 0 & 0 & (C_{11} - C_{12})/2 \end{bmatrix} \begin{bmatrix} \varepsilon_1 \\ \varepsilon_2 \\ \varepsilon_3 \\ \varepsilon_4 \\ \varepsilon_5 \\ \varepsilon_6 \end{bmatrix}$$

The above relation characterizes the anisotropic material known as transversely isotropic material. The transversely isotropic material has five independent elastic constants.

3.1.1.5 Isotropic Materials

Finally, if there exist infinite planes of material property symmetry, i.e., the material property is same in all possible directions, then the constitutive equation reduces to

$$\begin{bmatrix} \sigma_1 \\ \sigma_2 \\ \sigma_3 \\ \sigma_4 \\ \sigma_5 \\ \sigma_6 \end{bmatrix} = \begin{bmatrix} C_{11} & C_{12} & C_{12} & 0 & 0 & 0 \\ C_{12} & C_{11} & C_{12} & 0 & 0 & 0 \\ C_{12} & C_{12} & C_{11} & 0 & 0 & 0 \\ 0 & 0 & 0 & (C_{11} - C_{12})/2 & 0 & 0 \\ 0 & 0 & 0 & 0 & (C_{11} - C_{12})/2 & 0 \\ 0 & 0 & 0 & 0 & 0 & (C_{11} - C_{12})/2 \end{bmatrix} \begin{bmatrix} \varepsilon_1 \\ \varepsilon_2 \\ \varepsilon_3 \\ \varepsilon_4 \\ \varepsilon_5 \\ \varepsilon_6 \end{bmatrix}$$

The above relation characterizes the isotropic material. The isotropic material has only two independent elastic constants.

CHAPTER 4

WAVES IN ANISOTROPIC MEDIA

Wave propagation in anisotropic materials is significantly more complicated than in isotropic materials. The anisotropy in a material is caused by various factors such as fine layering, crystal/grain alignment or aligned fractures (Sinclair 2009). The material properties of an isotropic material are independent of the wave propagation direction. However, in an anisotropic material, material properties vary with the direction. Waves in anisotropic media (Auld 1990) does not propagate with spherical wavefront as it is known to exhibit in isotropic materials. Discussing the waves in a fully anisotropic (triclinic) material, let's assume an ultrasonic transducer attached to an anisotropic media emitting the ultrasonic field in the direction of k vector (Fig. 4.1a).

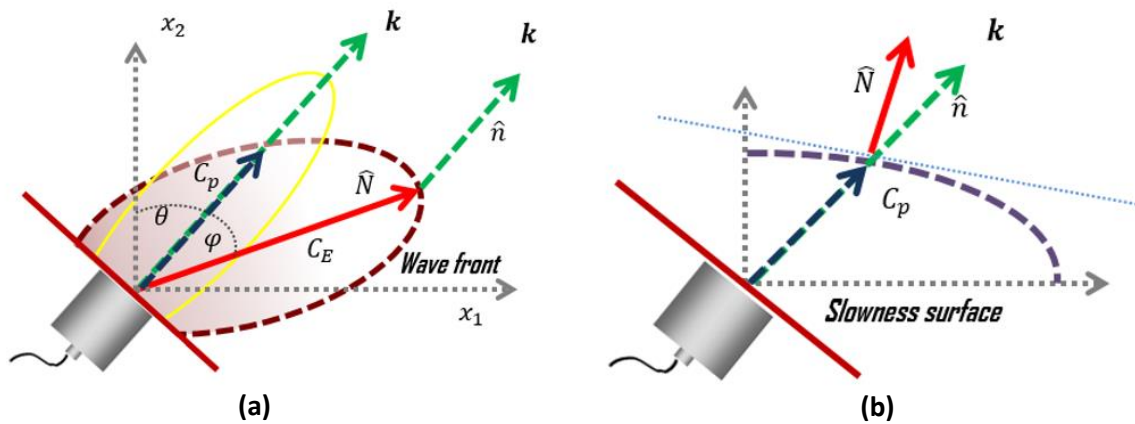


Fig. 4.1. An artistic view showing the schematics of the wave field inside a bulk anisotropic media a) showing the wavefront b) showing the slowness surface

If the wave is incident on an isotropic material, the wave energy propagates along the direction of the k vector. However, if the wave is incident on an anisotropic material, the wave does not propagate along k vector. Instead, the wave energy propagates along an entirely different direction creating a new wavefront. The wave propagation in anisotropic media is substantially different to the isotropic case in that elastic waves propagate with a velocity that is dependent on direction. Furthermore, unlike the isotropic case, three fundamental wave modes (Auld 1990, Rokhlin 2011) that propagate can be distinguished into one longitudinal and two shear waves. However, these modes are not necessarily pure modes as the particle vibration, or polarization (Lane 2014). It may be neither parallel nor perpendicular to the propagation direction. Hence, anisotropic modes are referred to as quasi-longitudinal and quasi-shear modes. The quasi-shear modes are further distinguished by their polarization: horizontal or vertical. The wave velocity for each of these modes is direction dependent. The wavefronts of these quasi-modes do not lie normal to the energy propagating direction and hence the phase and wave energy velocities do not coincide. It can be seen in fig 4.1a that the velocity of the wave energy, C_E is at an angle ϕ with respect to the phase velocity, C_P which is in the direction of the wave vector k . Also, the author would like to emphasize that the plane of energy propagation may or may not be on the same plane as the incident wave, i.e., the wave energy propagation direction represented by N vector may not be on the x_1 - x_2 plane. It can be along any direction in the 3D coordinate system based on the material properties and the direction of the k vector. Also, the Fig. 4.1b depicts the slowness surface which is obtained by plotting the inverse of the phase velocity along the direction of the wave propagation, i.e., k vector. The direction of

the wave energy propagation is represented by the normal to that slowness surface, i.e., \mathbf{n} . Hence the following understanding has been corroborated: in contrast to the phenomena in an isotropic material, the wavefront surfaces and the slowness surfaces are not concentric in the anisotropic material.

Now to further our understanding of different surfaces, i.e., how they are related and represented in the anisotropic material as well as for the visualization of those surfaces, we now focus on Fig. 4.2a. In an anisotropic material, the phase velocity and slowness are different and therefore a clear distinction between the two needs to be made. Velocity surface is the surface that is obtained by plotting the values of the modal wave velocities along the direction of the wave vector \mathbf{k} . In contrast, the slowness surface is a different surface, in comparison to the velocity surface, that is obtained by plotting the inverse of the wave velocity magnitudes along the same direction of wave vector \mathbf{k} . It is interesting to note that the wave energy propagation direction is represented by the normal to that slowness surface. Successively, the wavefronts can be obtained by plotting the equal energy lines in the media. The wavefront is propagated along the direction of the energy propagation as shown in the Fig. 4.1a, which is also the direction of the normal to the slowness surface as shown in Fig. 4.2a. The mathematical derivation essential to the proper understanding of the phenomena is discussed and explained later in this chapter.

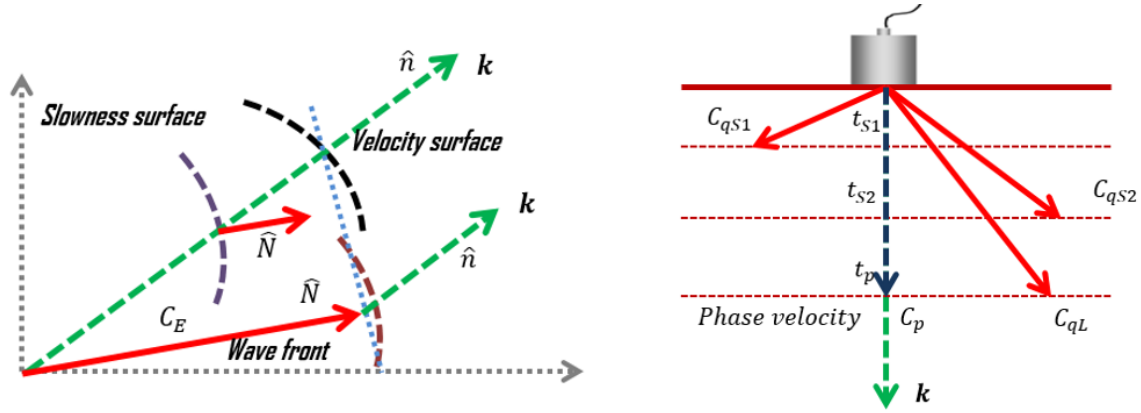


Fig. 4.2. a) Schematics of the wave surfaces and their relation b) relation of the phase velocity with the fundamental wave modes in anisotropic media.

Now with the help of Fig 4.2b, we try to visually understand the wave modes in the anisotropic media that have been discussed before. When the wave energy is introduced inside the anisotropic media, the wave breaks down into three fundamental modes (Auld 1990, Rokhlin 2011). They are quasi Longitudinal (qL), quasi Shear 1 or Quasi Slow Shear (qSS), and quasi Shear 2 or quasi Fast Shear (qFS). If the wave vector (k) represents the intended direction of the wave energy propagation in anisotropic media, the wave energy propagates in a different direction due to the modal wave velocities and the propagation direction being different for the above mentioned three wave modes. Also, the resultant phase velocity of the wave packet along the k direction is a summation of projection of the three wave modes (qL, qSS, and qFS) along the direction of the k vector which can be envisioned from Fig 4.2b.

With the theoretical knowledge gained until now, regarding the wave propagation behavior in anisotropic media, we can see that modeling the anisotropic wave field using the conventional ray tracing methods would be a formidable task. Hence, it can no longer be denied that a simplified and compact mathematical model, incorporating all the behavior mentioned above into the mathematical formulation, is needed for modeling the detailed and exact wave field.

4.1 Visualizing the Modal Wave Velocities

The fundamental elastodynamic equation (eq. 1) in anisotropic material (Auld 1990), which is also known as the equilibrium equation in solid medium, can be written as

$$\sigma_{ij,j} + f_i = \rho \ddot{u}_i \quad (1)$$

Where, σ_{ij} is the stress tensor, u_i is the displacement vector at a point in the solid, and f_i is the body force per unit volume. From the equation, we can see that the derivative of the stresses is related to the body force and the force due to the dynamic motions, following the Newton's second law. The stress is related to the strain in a linear elastic media (Rokhlin 2011) through their respective constitutive matrix equation (eq. 2). The material media is assumed linear since the wave has very short exposure time compared to the loading history of the material during the NDE inspection.

$$\sigma_{ij} = C_{ijml} \varepsilon_{ml} \quad (2)$$

Using the linear strain-displacement relation, the elastodynamic equation takes the following form regarding displacement (Banerjee and Kundu 2007) as shown in Eq. 3.

$$C_{ijml} \frac{\partial^2 u_m}{\partial x_j \partial x_l} + f_i = \rho \ddot{u}_i \quad (3)$$

Now, to comprehend the specifics and facts about the phenomena of anisotropic waves, we need to solve this complicated equation. Generally in an NDE experiment, a transducer which has a central actuation frequency is used. It implies that the transducer generates the maximum amplitude of the displacement at that frequency. However, there will be other proximal frequencies generating displacements with gradually lower amplitudes as well. Hence it is challenging, although not impossible, to be able to produce a monochromatic wave actuation with the help of ultrasonic transducer. In agreement to the assumption of linearity of the material, we know that the superposition theorem in the Fourier domain and the reciprocity theorem is valid. Thus, we can proceed to solve the above elastodynamic equation (eq. 3) using a monochromatic harmonic displacement function so that the solution is also valid for nearby frequencies generated by the transducer. Hence, assuming a monochromatic displacement function, we have

$$u_m = A g_m e^{i(\mathbf{k} \cdot \mathbf{x} - \omega t)} \quad (4)$$

Where, A , is the scalar amplitude of the wave, g_m is the polarization direction, ω is the monochromatic wave frequency, \mathbf{k} is the wave vector, \mathbf{x} is the position vector. In addition, $\mathbf{k} \cdot \mathbf{x}$ represents the dot product between \mathbf{k} and \mathbf{x} which signifies the phase component of the wave. Subsequent to the assumption of displacement function as above, substituting eq. 4 in to the eq. 3 and simplifying the mathematical expressions (Banerjee and Kundu 2007), we get the following equation eq. 5.

$$[C_{ijml} k_j k_l - \rho \delta_{im} \omega^2] A g_m = -f_i \quad (5)$$

To solve the above equation as an eigenproblem and acquire the eigenvalues and the eigenvectors of a system, we need to consider a homogeneous equation, i.e., the system under the absence of the forcing functions. To do so, we, therefore, proceed to set the body force to zero, i.e., there is no external force acting on the system at the moment. Thus, we beget the nontrivial solution of the equation which can be written as

$$[C_{ijml}n_jn_l - \rho\delta_{im}c^2]g_m = 0 \quad (6)$$

Where, $c^2 = \omega^2/k^2$ is the phase velocity of the wave along the direction of \mathbf{k} vector, n_j are the direction cosine of the wave propagation direction i.e., along the \mathbf{k} vector, and $C_{ijml}n_jn_l$ is the Christoffel acoustic tensor. By solving the above equation, we are able to obtain the phase velocities and the phase vectors of the three fundamental wave modes that are propagating in the material with material constants C_{ijml} .

The eq. 6 is well-known as Christoffel's equation (Christoffel 1877, Auld 1990) which, in our case, defines a set of three homogeneous linear equations for the polarization direction. Each of these equations constitutes an eigenvalue problem with its eigenvalues identified as c^2 along with the accompanying eigen vectors, g_m . Consequently, the solution of this equation will provide three eigen modes with wave velocities as C_{qL} , C_{qFS} and C_{qSS} , respectively, along the directions found from the eigen vectors. We are able to enhance our visual understanding with the help of Fig. 4.3. The solution is performed for a specific direction of wave propagation along the \mathbf{k} vector with direction normal \mathbf{n} . In a 3D coordinate system, the wave velocities are at the direction of their eigen vectors $\boldsymbol{\varphi}_L$, $\boldsymbol{\varphi}_{FS}$, $\boldsymbol{\varphi}_{SS}$, respectively. We are now able to visually and mathematically comprehend the physics

of the phase velocities. We can clearly see that the summation of projection of the phase velocities of the three wave modes on the \mathbf{k} vector gives the resultant phase velocity of the wave along \mathbf{k} . However, the wave energy propagation direction is in the direction of the resultant group velocity. In view of the mathematical derivation and understanding that followed in this section, we now are equipped with the tool to compute and determine the modal wave velocities due to wave actuation in any direction just by changing the \mathbf{n} vector pointing to any direction in the 3D coordinate system.

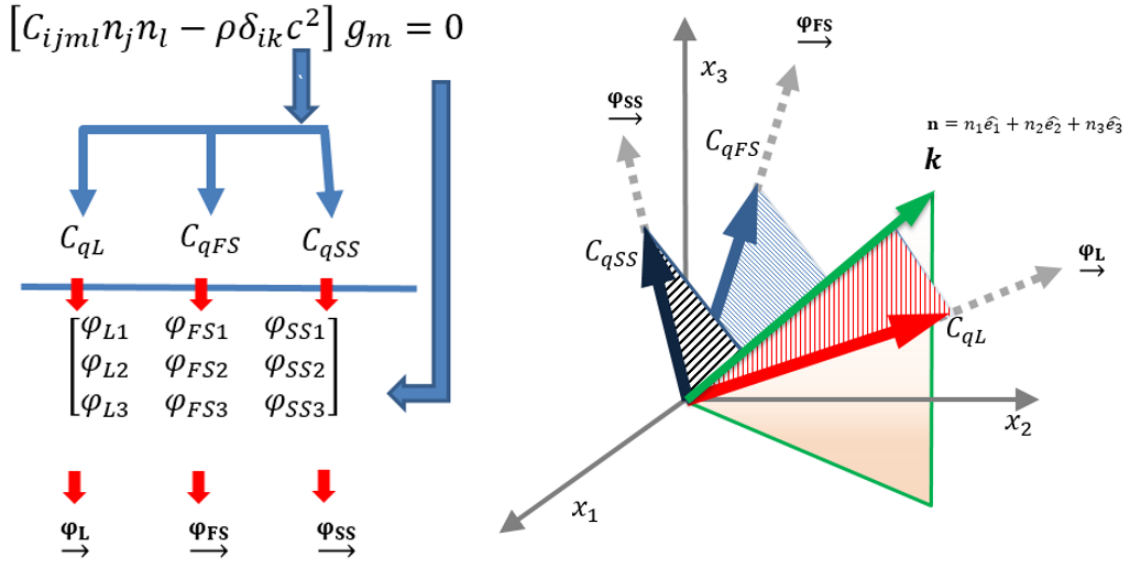


Fig. 4.3. Pictorial representation of the Christoffel's solution where the modal phase wave velocities are the eigenvalues and the direction of those wave modes are the eigenvectors.

4.2 Solution of Elastodynamic Green's Function

Now we have a clear understanding of the phase information associated with the wave modes in bulk anisotropic media. Hence, we want to move forward to our primary goal of simulating the anisotropic wave field with the help of virtual NDE experiment using DPSM. However, before we advance to do so, we need to compute the elastodynamic

Green's function in the anisotropic media (Yeatts 1984, Tverdokhlebov 1988, Kim, Every et al. 1994, Wang 1994, M., Schubert et al. 2000, Every, Pluta et al. 2004). In the upcoming portion of this section, we will see that the vital solution that we acquired by solving the Christoffel's equation is very crucial in the calculation of the Green's function.

Now to develop the mathematical formulation of the Green's function, we revisit the eq. 5. In contrast to transforming the equation into homogeneous in case of Christoffel's equation, we introduce an impulse force with the help of Dirac Delta function in the media due to a point source, which by definition contributes to the development of the solution of the elastodynamic Green's function. Based on this development, we modify the equation Eq. 5 to get the Cauchy-Navier Equation as shown below,

$$\left[C_{ijml} \frac{\partial^2}{\partial x_j \partial x_l} - \rho \delta_{im} \frac{\partial^2}{\partial t^2} \right] G_{mp}(x_n, t) = -\delta_{ip} \delta(x_n) \delta(t) F_p \quad (7)$$

where, $G_{mp}(x_n, t)$ is the time domain Green's function at x_n due to a point source actuation along the m -th direction with force amplitude F_p .

Afterwards, we acquire the governing elastodynamic equation to find the Green's function at a point x_n in the frequency-wavenumber domain by transforming the eq. 7 to the Fourier domain (\mathcal{F}) for both spatial and temporal variables as follows,

$$[C_{ijml} k_j k_l - \rho \omega^2 \delta_{im}] \tilde{G}_{mp}(k_n, \omega) = -\delta_{ip} \frac{1}{(2\pi)^3} f_p(\omega) \quad (8)$$

It is important to note that we used $\mathcal{F}[\delta(x_n)] = 1/(2\pi)^3$. Also, if we consider an operator that exist in the \mathcal{L}^2 Hilbert space, the above equation can be written as

$$\mathbf{L}_{im}\tilde{G}_{mp}(k_n, \omega) = \delta_{ip} \frac{1}{(2\pi)^3} f_p(\omega) \quad (9)$$

where,

$$\tilde{G}_{mp}(k_n, \omega) = \frac{1}{(2\pi)^4} \iiint_{-\infty}^{\infty} \int_{-\infty}^{\infty} G_{mp}(x_n, t) e^{i(k_l x_l - \omega t)} dx^3 dt \quad (10)$$

$$\mathbf{L}_{im}(k_n, \omega) = [C_{ijml} k_j k_l - \rho \omega^2 \delta_{ij}] \quad (11)$$

Now, we can further transform the dynamic equation in the frequency-wavenumber domain into the equation in the frequency-space domain by the application of inverse Fourier transform with respect to k_n . Thus, attained frequency domain Green's function in terms of the operator can be written as

$$g_{mp}(x_n, \omega) = \frac{1}{(2\pi)^3} \iiint_{-\infty}^{\infty} [\mathbf{L}_{mp}(k_n, \omega)^{-1}] e^{-ik_l x_l} dk^3 \quad (12)$$

As we can see that the above equation is pretty thought-provoking since it indicates that the Green's function at any point x_n in space will be the integral of all the possible wave numbers i.e. the total Green's function at any point x_n is the superposition of the influences of the waves propagating in all the possible directions. Hence it is essential to compute the wave field in all possible due to a point source.

4.3 Wave Modes in all possible wave directions in 3D

From the previous section, we were able to gain some understanding regarding the wave behavior in anisotropic media and the calculation of Green's function which is indispensable in the advancement of wave field modeling. We now know the superposition of all the waves propagating in all the possible directions is required for the computation of Green's function. We first want to explore the solution obtained by solving Eq. 6 from the section 3.1 and associate it with the term $\mathbf{L}_{im}(k_n, \omega)$ in the Eq. 12 so that we can physically realize and visualize the wave propagation in all possible direction for all three wave modes. By implementing the code in MATLAB to solve the Christoffel's equation, we obtain the eigenvalues and eigenvectors i.e. phase, velocities and phase vectors for each direction of propagation of the waves. The Christoffel's equation is solved for materials with various anisotropy such as isotropic, transversely isotropic, orthotropic, and monoclinic materials. We assume an anisotropic material with the material constants in the format shown below,

$$\begin{bmatrix} C_{11} & C_{12} & C_{13} & C_{14} & C_{15} & C_{16} \\ C_{21} & C_{22} & C_{23} & C_{24} & C_{25} & C_{26} \\ C_{31} & C_{32} & C_{33} & C_{34} & C_{35} & C_{36} \\ C_{41} & C_{42} & C_{43} & C_{44} & C_{45} & C_{46} \\ C_{51} & C_{52} & C_{53} & C_{54} & C_{55} & C_{56} \\ C_{61} & C_{62} & C_{63} & C_{64} & C_{65} & C_{66} \end{bmatrix}$$

By solving for the wave slowness which is the inverse of the wave velocities in all possible direction of the wave propagation by discretizing a sphere, we can compare and differentiate the dissimilarity in the wave behavior in materials of different orders of

anisotropy. To do so, we select the materials with following material properties which are as follows.

a) Orthotropic, Transversely Isotropic with material properties $C_{11} = 143.8 \text{ GPa}$, $C_{12} = C_{13} = 6.2 \text{ GPa}$, $C_{22} = 13.3 \text{ GPa}$, $C_{23} = 6.5 \text{ GPa}$, $C_{33} = 13.3 \text{ GPa}$, $C_{44} = 3.4 \text{ GPa}$, $C_{55} = C_{66} = 5.7 \text{ GPa}$ and density, $\rho = 1560 \text{ Kg} / \text{m}^3$

b) Fully Orthotropic material with material properties $C_{11} = 70 \text{ GPa}$, $C_{12} = 23.9 \text{ GPa}$, $C_{13} = 6.2 \text{ GPa}$, $C_{22} = 33 \text{ GPa}$, $C_{23} = 6.8 \text{ GPa}$, $C_{33} = 14.7 \text{ GPa}$, $C_{44} = 4.2 \text{ GPa}$, $C_{55} = 4.7 \text{ GPa}$, $C_{66} = 21.9 \text{ GPa}$ and density, $= 1500 \text{ Kg} / \text{m}^3$

c) Monoclinic material with material properties, material properties $C_{11} = 102.6 \text{ GPa}$, $C_{12} = 24.1 \text{ GPa}$, $C_{13} = 6.3 \text{ GPa}$, $C_{16} = 40 \text{ GPa}$, $C_{22} = 18.7 \text{ GPa}$, $C_{23} = 6.4 \text{ GPa}$, $C_{26} = 10 \text{ GPa}$, $C_{33} = 13.3 \text{ GPa}$, $C_{36} = -0.1 \text{ GPa}$, $C_{44} = 3.8 \text{ GPa}$, $C_{45} = 0.9 \text{ GPa}$, $C_{55} = 5.3 \text{ GPa}$, $C_{66} = 23.6 \text{ GPa}$ and density, $= 1560 \text{ Kg} / \text{m}^3$

The four different types of slowness plots are presented for each mode, i.e., quasi-longitudinal (QL), quasi-shear 1 (QS1) and quasi-shear 2(QS2) and compared to the wave velocity slowness of the longitudinal and two shear wave modes in aluminum, which is an isotropic material. The plots depict the slowness behavior in 3D surface plot and contour plots in three different planes, i.e., X-Y contour plot, Y-Z contour plot and X-Z contour plot. The 3D plot is color-coded to for the better visualization of the magnitude of the phase slowness with red being the highest and blue being the lowest magnitude. The QL contour plot is color-coded red, QS1 contour plot is color-coded green, QS1 contour plot is color-coded blue.

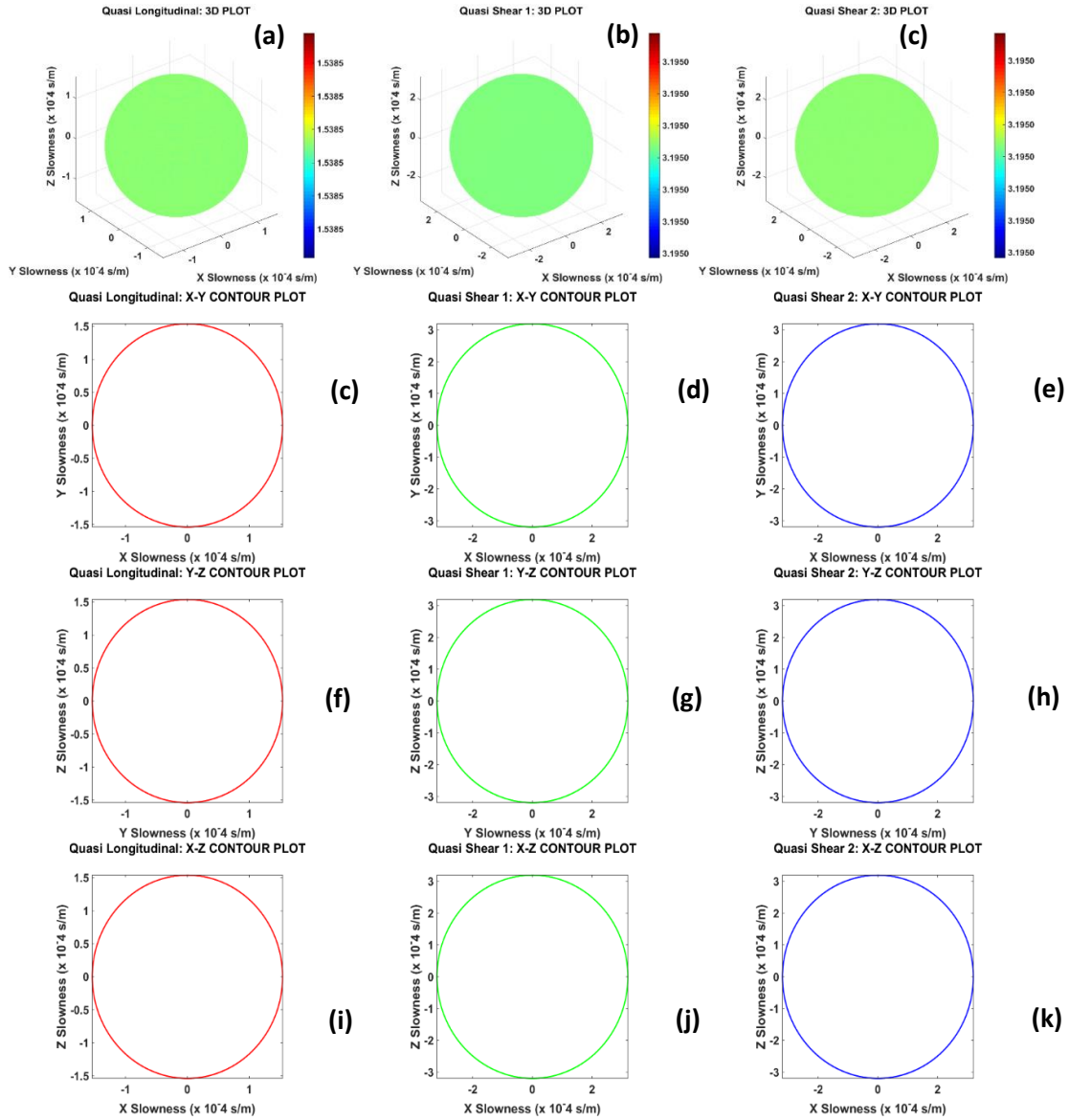


Fig. 4.4. For Aluminum, 3D slowness plot: a) quasi-longitudinal mode b) quasi-slow shear (qS1) mode and c) quasi-fast shear (qS2) mode. X-Y Contour plot: d) quasi-longitudinal mode e) quasi-slow shear (qS1) mode and f) quasi-fast shear (qS2) mode. Y-Z Contour plot: g) quasi-longitudinal mode h) quasi-slow shear (qS1) mode and i) quasi-fast shear (qS2) mode. X-Z Contour plot: j) quasi-longitudinal mode k) quasi-slow shear (qS1) mode and l) quasi-fast shear (qS2) mode.

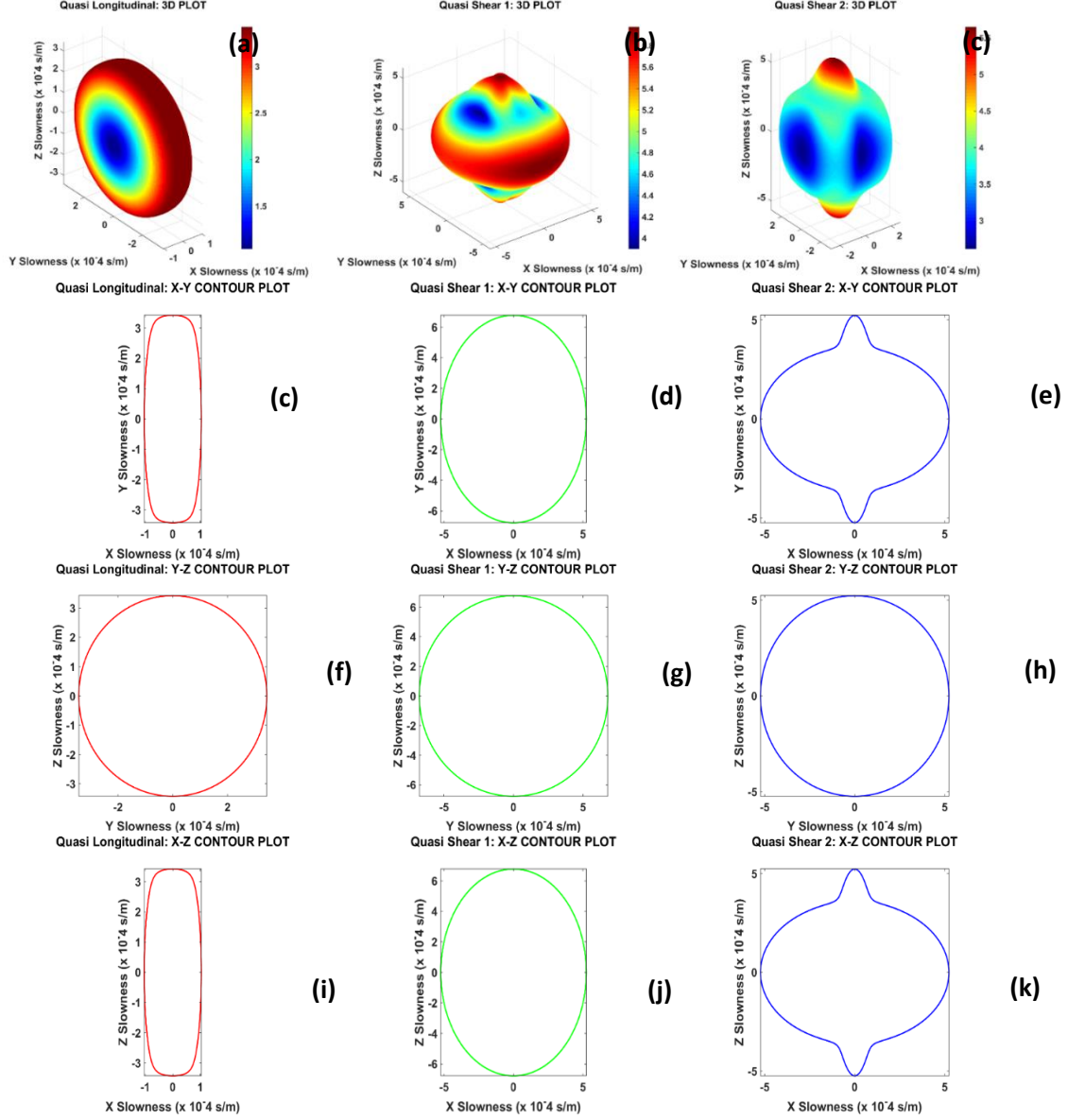


Fig. 4.5. For Transversely Isotropic Material, 3D slowness plot: a) quasi-longitudinal mode b) quasi-slow shear (qS1) mode and c) quasi-fast shear (qS2) mode. X-Y Contour plot: d) quasi-longitudinal mode e) quasi-slow shear (qS1) mode and f) quasi-fast shear (qS2) mode. Y-Z Contour plot: g) quasi-longitudinal mode h) quasi-slow shear (qS1) mode and i) quasi-fast shear (qS2) mode. X-Z Contour plot: j) quasi-longitudinal mode k) quasi-slow shear (qS1) mode and l) quasi-fast shear (qS2) mode.

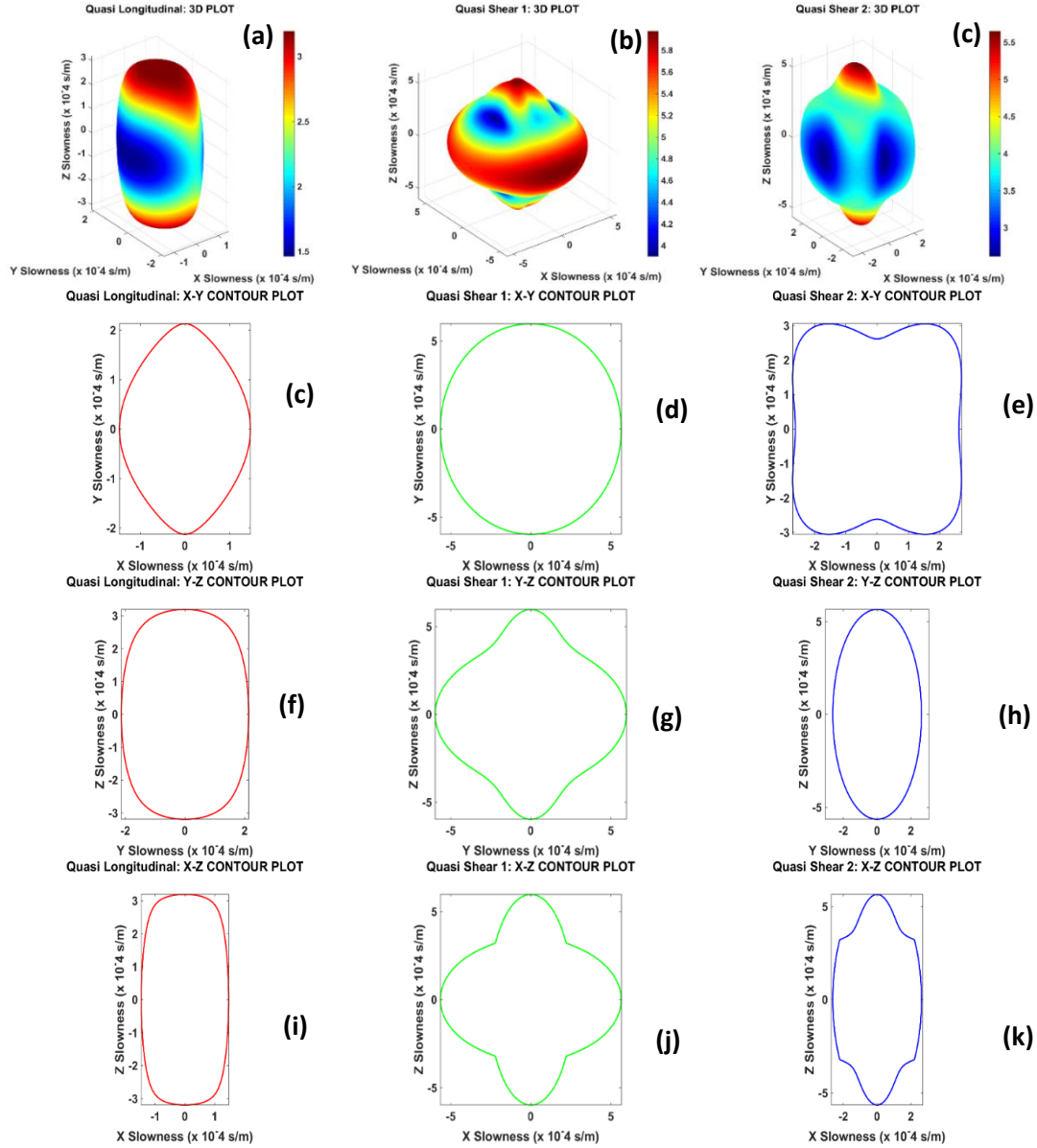


Fig. 4.6. For Orthotropic Material, 3D slowness plot: a) quasi-longitudinal mode b) quasi-slow shear (qS1) mode and c) quasi-fast shear (qS2) mode. X-Y Contour plot: d) quasi-longitudinal mode e) quasi-slow shear (qS1) mode and f) quasi-fast shear (qS2) mode. Y-Z Contour plot: g) quasi-longitudinal mode h) quasi-slow shear (qS1) mode and i) quasi-fast shear (qS2) mode. X-Z Contour plot: j) quasi-longitudinal mode k) quasi-slow shear (qS1) mode and l) quasi-fast shear (qS2) mode

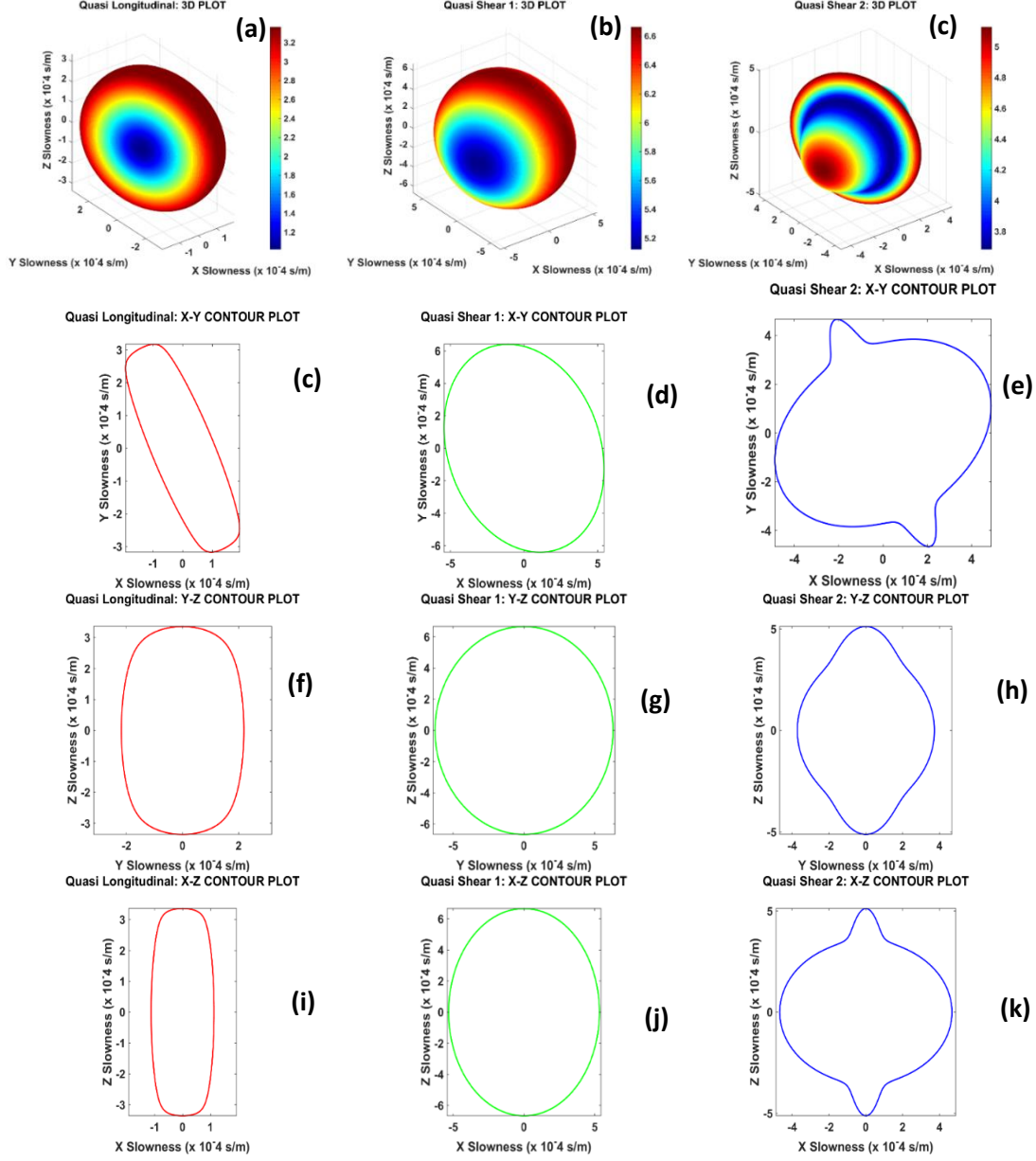


Fig. 4.7. For Monotropic Material, 3D slowness plot: a) quasi-longitudinal mode b) quasi-slow shear (qS1) mode and c) quasi-fast shear (qS2) mode. X-Y Contour plot: d) quasi-longitudinal mode e) quasi-slow shear (qS1) mode and f) quasi-fast shear (qS2) mode. Y-Z Contour plot: g) quasi-longitudinal mode h) quasi-slow shear (qS1) mode and i) quasi-fast shear (qS2) mode. X-Z Contour plot: j) quasi-longitudinal mode k) quasi-slow shear (qS1) mode and l) quasi-fast shear (qS2) mode

From the comparison of the phase slowness surfaces between the isotropic and anisotropic material, we see that while the slowness surfaces are spherical in an isotropic

material, they are non-spherical in an anisotropic material. Also, it is important to note that the slowness profile is circular in y-z plane of the transversely isotropic material (Fig. 4.6 a, f, g, h) which is expected. The same circular profile is realized in a monoclinic material with a skewed axis of symmetry. In agreement with our theoretical understanding, we can verify the symmetry of the phase slowness about X-axis in the transversely isotropic material due to YZ being the plane of isotropy and no symmetry of the phase slowness along any axes in the orthotropic material.

Furthermore, we will see that this information regarding 3D wave slowness for all wave modes are critical for the calculation of 3D Green's function in the materials in the upcoming section.

4.4 Exact Mathematical Expression for the Green's Function

In section 3.2, by the application of Fourier transformation, we were able to gain some physical and mathematical meaning of the Green's function. However, by looking at the eq. 12, we can see that the equation is still not in the form which can be effortlessly implemented into the computer code. Hence, our next step is to solve the Green's function equation and develop a more convenient form such that we can compute the Green's function in frequency domain. To achieve that, in this section, we are going to utilize few techniques and theorem and find the mathematical expression of the Green's function which can be used in the numerical computation and modeling of the wave field. Also, the meaning of essential terms for the calculation of the Green's function will be explained along with the derivation. About developing this new form of Green's function equation,

we now treat the equation Eq. 7 with a different process, i.e., instead of applying the Fourier transform to space and time both we just transform the equation to the frequency domain.

$$\left[C_{ijml} \frac{\partial^2}{\partial x_j \partial x_l} + \rho \omega^2 \delta_{im} \right] g_{mp}(x_n, \omega) = -\delta_{ip} \delta(x_n) f_p(\omega) \quad (14)$$

By the observation of the frequency domain Green's function in Eq. 14, we see that the equation is a second order partial differential equation and it is common knowledge that solving such higher order partial differential equation is an intricate task. Therefore, we need to find such a method that can transform these complex partial differential equations into a set of simple ordinary differential equations so that it can be solved without difficulty.

One such method that we propose to use in this thesis work is called Radon's transform method (Deans 2007). Radon's transform is an elegant technique that helps in transformation of any 3D images into 2D planes and any 2D image into 1D line. Hence, this technique is heavily applied in the field of computed tomography (CT) and 3D image reconstruction from a cluster of 2D projection images taken on different planes. The transformation of 3D function into multiple functions projected on 2D planes is made possible by Radon transform by the parameterization of the orientation of the planes. Contrary to that, the transformation of images on the 2D planes to a 3D image is made possible by inverse Radon transform. Hence in our case, a forward radon transform is utilized in transferring a 3D function to a 2D function, parameterized by the definition of the 2D planes.

Now let's proceed to the underlying mathematical understanding of Radon transform.

Assuming x_1, x_2 and x_3 are the coordinates of a point (\mathbf{x}) in a Euclidean space \mathbb{R}^3 , Radon

transform (Banerjee and Kundu 2007) of any function $g(\mathbf{x})$, which is defined and absolutely integrable over all space, can be written as

$$\tilde{g}(\vec{\mu}, h) = R\{g(\vec{x})\} = \int g(\mathbf{x})\delta(h - \vec{\mu} \cdot \vec{x})d\Omega \quad (15)$$

Where $d\Omega$ is the volume element and equation (15) is a surface integral over the plane $h = \mu_k x_k$. The physical meaning of the integral could be briefly described in 2D and 3D using the Fig. 4.8. In case of 2D, the infinite numbers of lines can be defined as the function of distance h from the origin with their local orientation of the lines designated by their unit normal $\vec{\mu}$ such that each line can be represented by a point in the Radon space. Similarly, in case of 3D, the infinite numbers of planes can be defined as the function of distance h from the origin with their local orientation of the planes designated by their unit normal $\vec{\mu}$ such that 3D image can be represented by a 2D plane in the Radon space. The Dirac δ function in eq. 15 signifies that the values exist only on the plane $\vec{\mu}, h$ and everywhere else the integral ceases to exist, i.e., it is zero.

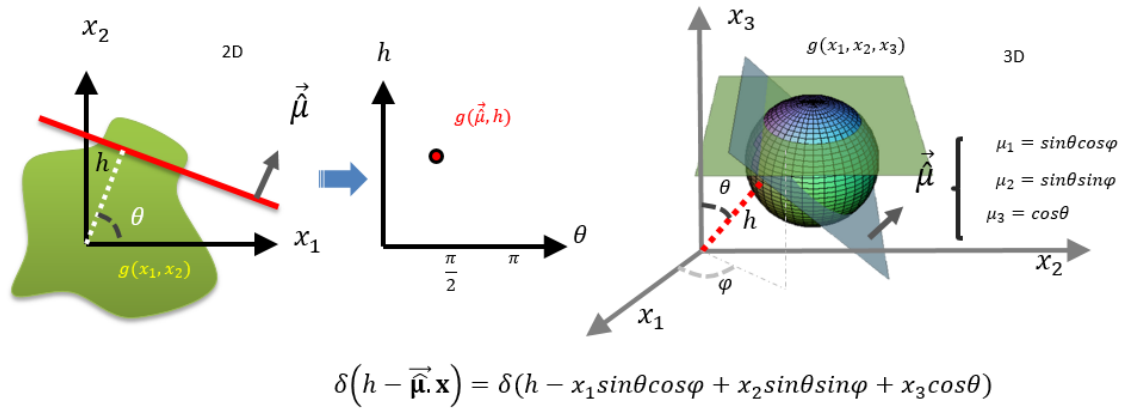


Fig. 4.8. A schematic diagram to visualize the Radon transform in 2D and 3D. The figure shows that the integral is performed over a circular domain with different radius in 2D and over a sphere with different radius in 3D.

Radon transform has many elegant features. However, here we mention few of them that was adopted in the process of transforming the partial differential equation (Eq. 14) into the coupled ordinary differential equations. Those features are as follows.

Radon transform of derivatives of a function (Wang 1994) can be written as

$$R\left\{\left(\frac{\partial^2 g}{\partial x_i \partial x_j}\right)\right\} = \mu_i \mu_j \frac{\partial \tilde{g}(h, \boldsymbol{\mu})}{\partial h^2} \quad (16)$$

Moreover, the inverse Radon transform of the above equation (Wang 1994) can be written as

$$g(\mathbf{x}, \omega) = -\frac{1}{8\pi^2} \iiint_{|\boldsymbol{\mu}|=1}^{sphere} \left. \frac{\partial^2 \tilde{g}(h, \boldsymbol{\mu})}{\partial h^2} \right|_{h=\boldsymbol{\mu} \cdot \mathbf{x}} d\Omega(\boldsymbol{\mu}) \quad (17)$$

We use these identities in our forthcoming calculations. After applying the Radon transform on the eq. 14 we get coupled ordinary differential equations.

$$\Gamma_{im} \frac{d^2 \tilde{g}_{mp}}{dh^2} + \omega^2 \delta_{im} \tilde{g}_{mp} = -\delta_{ip} \frac{f_p(\omega)}{\rho} \delta(h) \quad (18)$$

$$\Gamma_{im} = \frac{c_{ijml} \mu_j \mu_l}{\rho} ; B_{mj} B_{jp} = \omega^2 \Gamma_{im}^{-1} \quad (19)$$

By looking the set of ordinary differential equations (eq. 18), we can realize that the Eigenvalue solution is required in solving those equations. However, it is quite fortunate that we have already addressed the needed Eigensolution or the phase information using the equation in Eq. 6. Besides, the wave propagation direction pointed by the direction cosine n_i in eq. 6 are equivalent to the direction cosine of the plane used for integration in Radon transform in eq. 16. The solution (Yeatts 1984) of the eq. 18 can be written as,

$$\tilde{g}_{mp} = \frac{i}{\omega^2 \rho} f_p B_{jp} e^{ihB_{mj}} ; h > 0 \quad (20)$$

Further applying the spectral theorem, we can write an analytic function \mathbf{L} which is a function of the Γ_{im} matrix in the following form

$$\mathbf{L}(\Gamma_{im}) = \sum_{z=1}^n \mathbf{L}(\gamma_z) (P_{im})^{(z)} \quad (21)$$

Where z is the index is eigenvalues for the summation and n is the total number of eigenvalues in the system. Since in our case we have three eigenvalues, hence $n = 3$. γ_z is the z -th eigen value and $(P_{im})^{(z)}$ is the projection matrix of the z -th eigen mode. The correspondence between the eigen modes with the wave velocities C_{qL} , C_{qFS} , C_{qSS} , their eigen vectors $\boldsymbol{\varphi}_L$, $\boldsymbol{\varphi}_{FS}$, $\boldsymbol{\varphi}_{SS}$, respectively and the new parameter defined as γ_z and $(P_{im})^{(z)}$ can be explicitly written as follows

$$\gamma_1 = (C_{qL})^2 ; \gamma_2 = (C_{qFS})^2 ; \gamma_3 = (C_{qSS})^2 \quad (21)$$

$$(P_{im})^{(1)} = \varphi_{Li} \varphi_{Lm} ; (P_{im})^{(2)} = \varphi_{FSi} \varphi_{FSm} ; (P_{im})^{(3)} = \varphi_{SSi} \varphi_{SSm} \quad (22)$$

Based on these understanding, by the application of spectral resolution theorem, we can further write the analytic transformed displacement function as

$$\tilde{g}_{mp} = \frac{i}{\omega^2 \rho} f_p \sum_{z=1}^3 \frac{\omega}{\sqrt{\gamma_z}} e^{ih(\frac{\omega}{\sqrt{\gamma_z}})} (P_{mp})^{(z)} \quad (23)$$

Now applying the inverse Radon transform, we get the displacement Green's function (Yeatts 1984) in the frequency domain

$$g_{mp}(x_n, \omega) = \frac{i\omega}{8\pi^2 \rho} f_p \sum_{z=1}^3 \iiint_{|\boldsymbol{\mu}|=1}^{sphere} H_z(\mu_i x_i) \frac{1}{\gamma_z \sqrt{\gamma_z}} (P_{mp})^{(z)} e^{ih(\frac{\omega \mu_i x_i}{\sqrt{\gamma_z}})} d\Omega(\boldsymbol{\mu}) \quad (24)$$

Where, $H_z(\mu_i x_i)$ is the Heaviside step function which implies that the integral only exists for $\mu_i x_i \geq 0$ and it vanishes for $\mu_i x_i < 0$. Hence the integral in eq. 24 is valid only when the angle between the direction of wave propagation and the Radon's plane is less than or equal to 90° . To add to that, we can say that the intended direction between a source and a target and the reduced 2D Radon planes will make a hemisphere, inside which the integral (eq. 24) is valid. This equation ep. 24 is the expression for the displacement Green's function in frequency domain.

However, we want an even more simplified expression for the Green's function. To achieve that, we shall revisit the eq. 12. By substituting the corresponding relation discussed in eq. 21 and applying the spectral theorem, following the simplification, we can express the inverse of the Christoffel's operator $\mathbf{L}_{mp}(k_n, \omega)$ as follows

$$\mathbf{L}_{mp}(k_n, \omega)^{-1} = \sum_{z=1}^3 \frac{\varphi_{mi}^{(z)} \varphi_{ip}^{(z)}}{\rho \gamma_z |k|^2 - \rho \omega^2} = \sum_{z=1}^3 \frac{\gamma_z^{-1} (P_{mp})^{(z)}}{\rho (|k|^2 - \omega^2 / \gamma_z)} \quad (25)$$

By substituting Eq. 25 into the Eq. 12, we get an alternative expression for the displacement Green's function which we can write as follows.

$$g_{mp}(x_n, \omega) = \frac{f_p}{(2\pi)^3} \sum_{z=1}^3 \iiint_{\substack{sphere \\ |\mathbf{r}|=1}} [(s_z)^2 (P_{mp})^{(z)} \sin\theta d\theta d\phi] \times \int_{-\infty}^{\infty} \left[\frac{\exp(-i|k| x_1 \sin\theta \cos\phi + x_2 \sin\theta \sin\phi + x_3 \cos\theta)}{(|k|^2 - \omega^2 (s_z)^2)} \right] k^2 dk \quad (26)$$

We can see that the above equation is explicitly in the spherical coordinate system. The Green's equations represented by Eq. 24 and Eq. 26 must be equal as one is just an alternative form of the other.

However, in eq. 26, the latter part of the integral has a pole at $|k|^2 = a^2$, where $a = \omega s_z$ which can be simplified by the application of the following identity known as Cauchy's integral formula (Every, Pluta et al. 2004).

$$\int_{-\infty}^{\infty} \frac{\exp(iku)}{(k^2 - a^2)} k^2 dk = \pi i a e^{ia|u|} + 2\pi\delta(u) \quad (27)$$

Substituting the Cauchy's integral identity (Eq. 27) into Eq. 26 and performing mathematical simplifications, we get the final expression for the displacement Green's functions in the frequency domain.

$$g_{mp}(x_n, \omega) = \frac{i\omega f_p}{2(2\pi)^2 \rho} \sum_{z=1}^3 \int_{r=0}^{r=1} \int_{\theta=0}^{\theta=\pi} \int_{\phi=0}^{\phi=2\pi} \left[(s_z)^3 (P_{mp})^{(z)} \exp(i(k_i x_i)^{(z)}) \sin\theta d\theta d\phi \right] \\ + \frac{1}{2(2\pi)^2 \rho |x|} \int_0^{2\pi} (s_z)^2 (P_{mp})^{(z)} d\phi \quad (28)$$

In the final expression above, we can see that the Green's function is calculated by integrating over the sphere and summing all three wave modes such that it incorporates the influence of all the wave propagation in all possible direction. For the visual understating of the expression, we look into the representative figure (Fig 4.9) below.

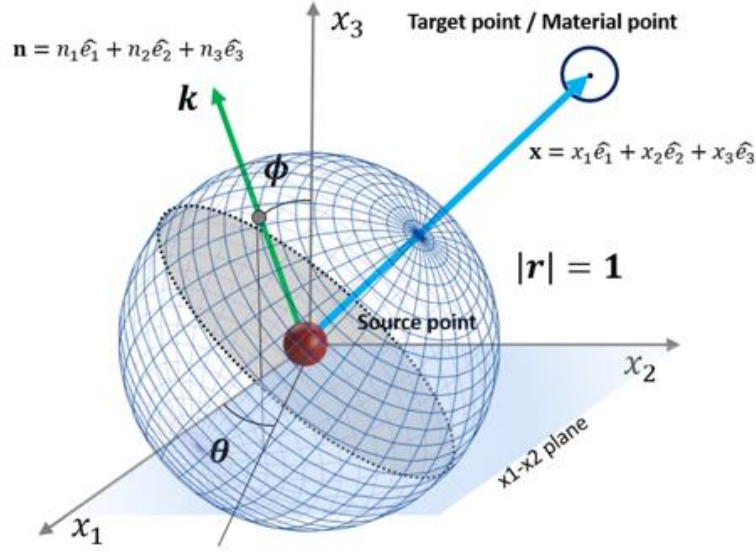


Fig 4.9. A schematic diagram to visualize the integral in Eq. 28.

It is required to calculate the wave field in the intended direction of wave propagation (blue arrow) at any target point (black dot with blue ring) due to any source point (red sphere). For that purpose, the influence of the wave field at the target due to all three wave modes in all possible wave direction (green arrow) is considered. Also, only the forward propagating waves, i.e., the grid points on the sphere above the midplane (gray plane) are considered which is similar to the existence of Heaviside step function in Eq. 24. Furthermore, the normal to the gray plane can be visualized as a radon plane $h = \mu_k x_k$ in Fig. 4.9 where μ_k is identical to n_k . The second part of the integral in Eq. 28 pertains to the perimeter of the circle on the midplane (gray plane) perpendicular to the blue arrow.

After the computation of displacement Green's function, we proceed to compute the stress Green's function. Moreover, for that, we change our nomenclature of displacement Green's function to avoid the confusion in the derivation and the simplicity

of understanding of the equation; we write $g_{mp} = u_m^p$. Before we can calculate the stress Green's Function, we need to calculate the strain.

The strains at the target point can be calculated with the help of strain-displacement relation which requires taking the spatial derivative of the displacement Green's functions obtained from the eq. 28. The expression is as follows.

$$\varepsilon_{mj}^p = \frac{1}{2} (u_{m,j}^p + u_{j,m}^p) \quad (29)$$

Finally, to calculate the stress Green's Function tensor for a specific direction of point force along p , we will use the constitutive equation for the anisotropic medium given by,

$$\sigma_{ik}^p(\mathbf{x}) = C_{ikmj} \varepsilon_{mj}^p(\mathbf{x}) \quad (30)$$

Where, σ_{ik}^p is the stress tensor at the target point (\mathbf{x}) due to the source point with force along the p -th direction.

Hence, we finally have both the displacement and stress Green's Functions required for the modeling of the wave field in anisotropic media.

CHAPTER 5

NUMERICAL COMPUTATION OF GREEN'S FUNCTION

Now that we have the mathematical derivation required for the calculation of the displacement and stress Green's Functions, we can proceed with the modeling of the wave field in anisotropic media. However, before that, we want to make sure that the implementation of Green's function into MATLAB code is verified. Also, we also want to understand the physical meaning of the Green's function as well as visualize the behavior of materials with different types of anisotropy. Therefore, we first calculate the Green's function for materials that we already considered in chapter 3, a) Transversely isotropic, b) Fully orthotropic, c) Monoclinic material and compare it to the isotropic material, aluminum to see the difference between the isotropic and anisotropic material. For that purpose, we consider two geometric configurations as shown in Fig. 5.1.

In the Fig. 5.1a, we have a configuration for calculation of the displacement Green's function along a straight line inside the materials. The configuration is composed of eleven target points with a spacing of 1mm and point source with an excitation frequency of 1MHz. The target points and point source is separated by a distance of 10mm. The displacement Green's function is numerical computed and plotted along the line of target points.

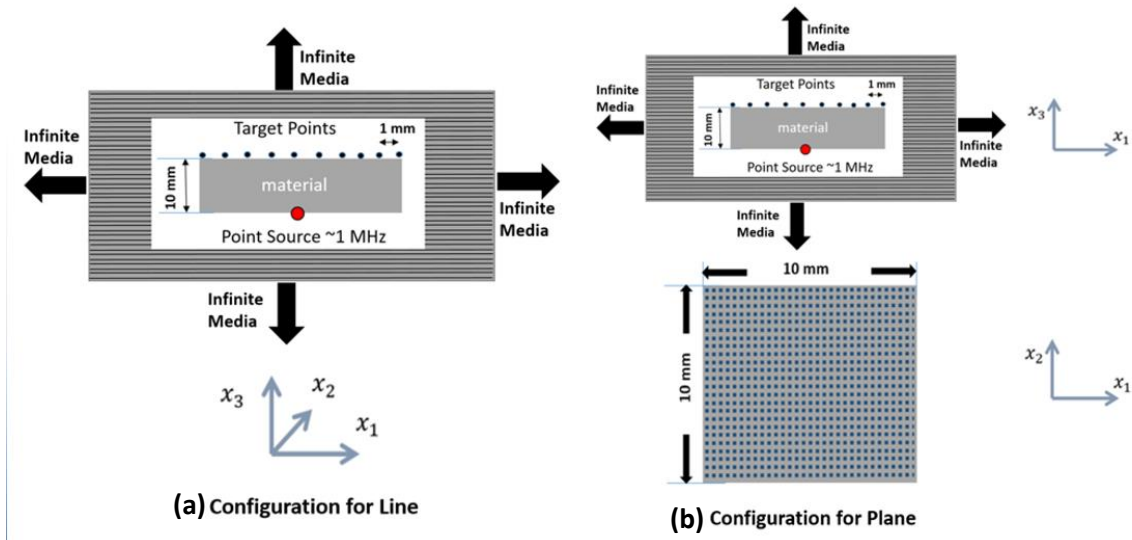


Fig. 5.1. Schematics of configurations to calculate the Green's function a) for a line b) for a plane

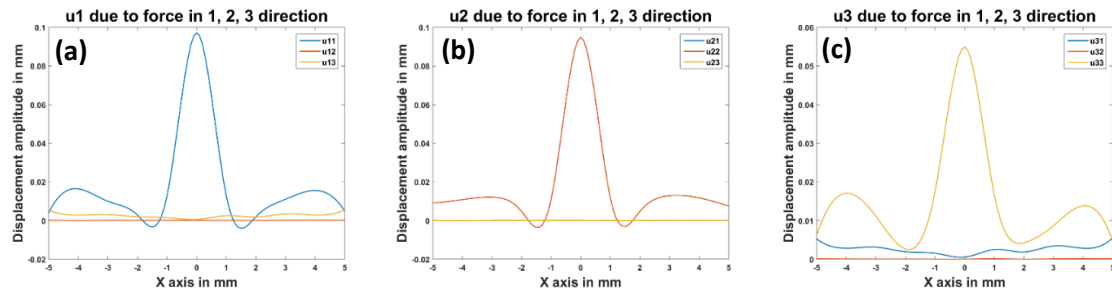


Fig. 5.2. Numerical computation of displacement Green's function (unit mm) due to forces acting along 1, 2 & 3 directions in Fig 5.1a when the inside material is Isotropic. a) displacements along x_1 direction, b) displacements along x_2 direction c) displacements along x_3 direction

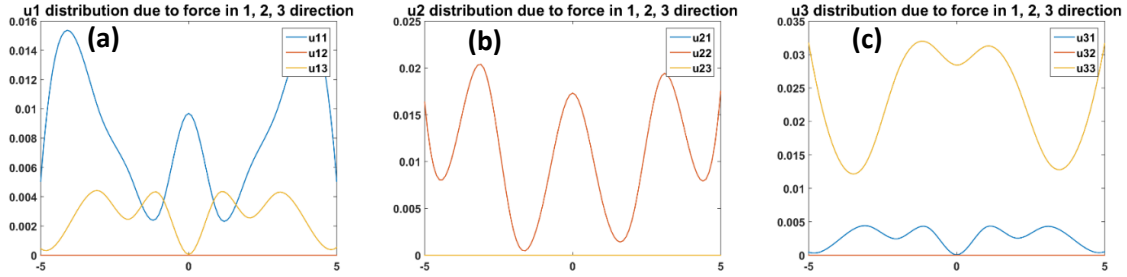


Fig. 5.3. Numerical computation of displacement Green's function (unit mm) due to forces acting along 1, 2 & 3 directions in Fig 5.1a when the inside material is Transversely Isotropic. a) displacements along x_1 direction, b) displacements along x_2 direction c) displacements along x_3 direction

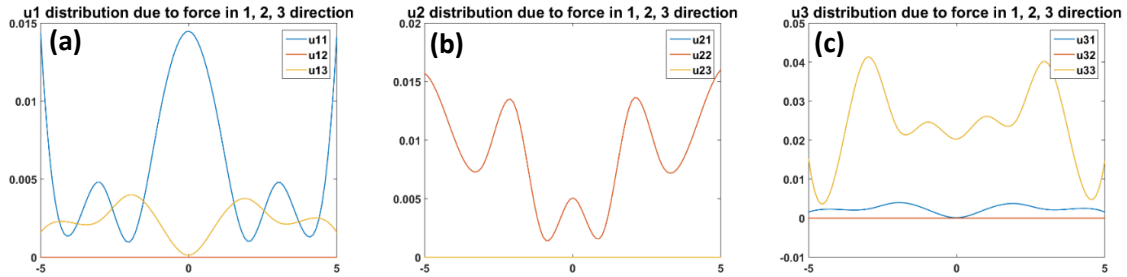


Fig. 5.4. Numerical computation of displacement Green's function (unit mm) due to forces acting along 1, 2 & 3 directions in Fig 5.1a when the inside material is Fully Orthotropic. a) displacements along x_1 direction, b) displacements along x_2 direction c) displacements along x_3 direction

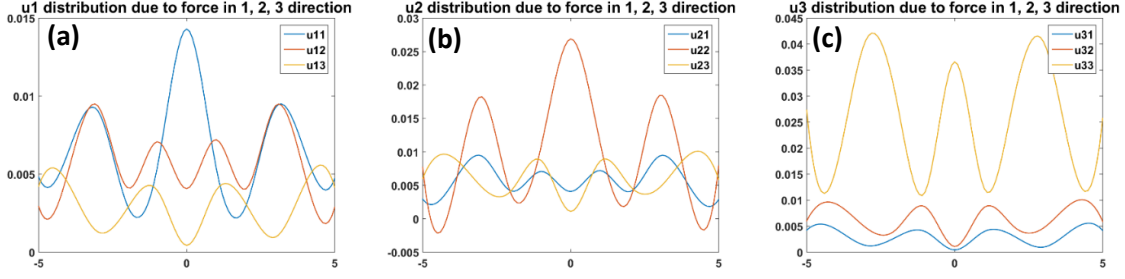


Fig. 5.5. Numerical computation of displacement Green's function (unit mm) due to forces acting along 1, 2 & 3 directions in Fig 5.1a when the inside material is Monoclinic. a) displacements along x_1 direction, b) displacements along x_2 direction c) displacements along x_3 direction

If we look at the displacement Green's function plot for line configuration (fig 5.2 – 4.5), we see that for the isotropic material, the displacements are maximum at the center, i.e., at the closest proximity to the point source actuation and decays along either side. Similarly, for the transversely isotropic material assuming a composite, the displacements are not maximum at the center. Instead, it bifurcates along the fiber direction. Also, we can see the various behavior depicted by the orthotropic and monoclinic material. Since the behavior illustrated agree to our theoretical understanding of the material, the implementation of Green's function is verified.

Now to further enhance our numerical computation and understanding of the Green's function, we calculate the Green's function for a plane or rectangular domain. In the Fig. 5.1 b, we have a configuration for calculation of the displacement and stress Green's function in an arbitrary plane inside the Transversely Isotropic material. The configuration is composed of 51 X 51 target points with a spacing of 1mm in a square plane of 10 mm X 10 mm and point source with an excitation frequency of 1MHz. The plane of target points and point source is separated by a distance of 2 mm. The stress and

displacement Green's function is numerical computed and plotted as a contour plot along the plane of target points.

Based on the displacement and stress Green's functions (Fig. 5.6 – 5.8), we were able to understand that the Green's function represents the influence of the source with unit load at any arbitrary target point in the space as well as its dependency on the material property. Also, we also enriched our numerical computation and can finally progress with the calculation of ultrasonic wave field in an anisotropic solid, when the bounded ultrasonic beam is generated from 1 MHz ultrasonic transducer.

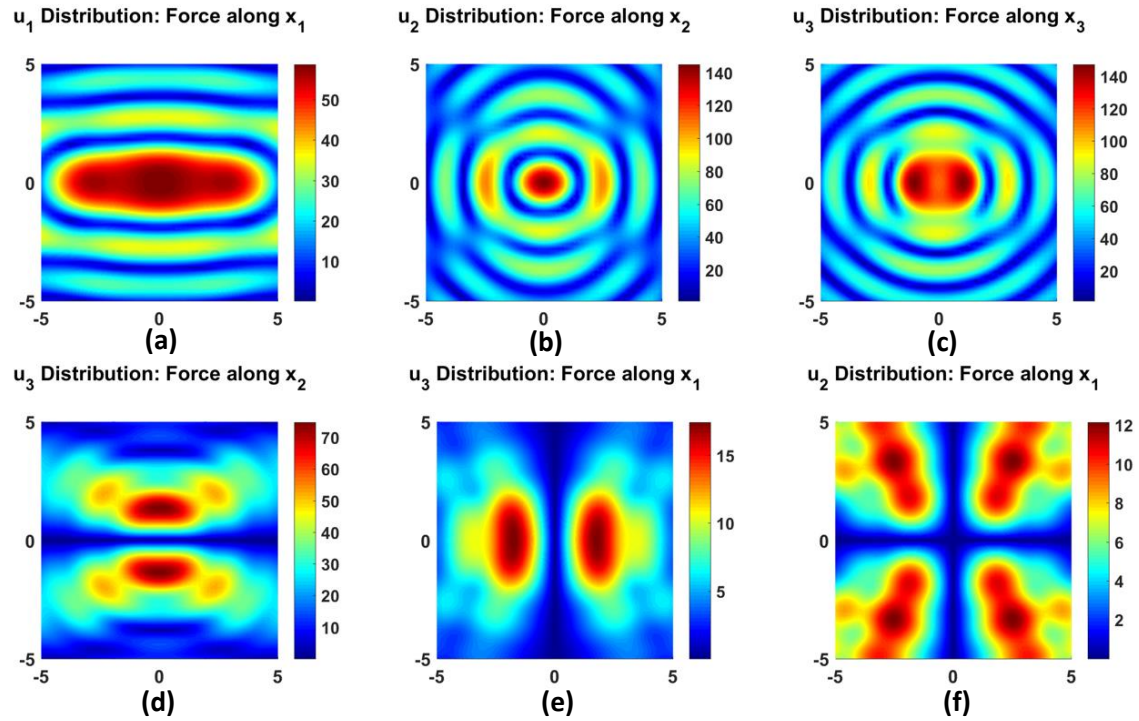


Fig.5.6. Numerical computation of displacement Green's function (unit mm) in Transversely Isotropic material a) g_{11} b) g_{22} c) g_{33} d) g_{31} or g_{13} e) g_{32} or g_{23} f) g_{21} or g_{12}

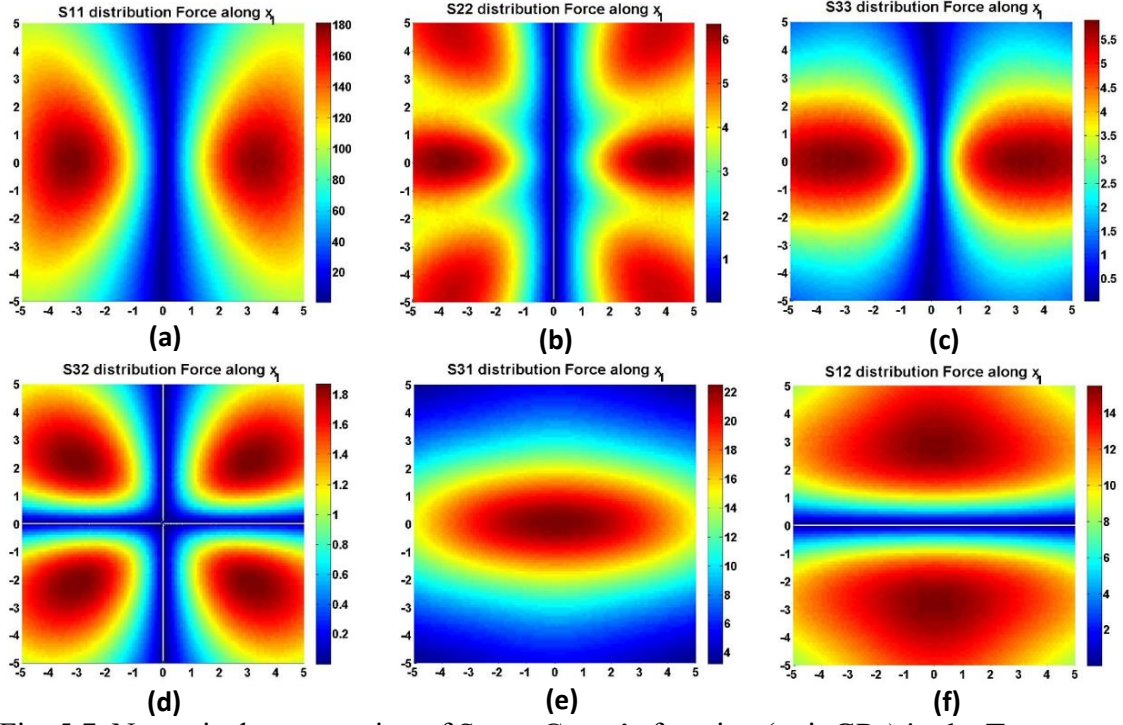


Fig. 5.7. Numerical computation of Stress Green's function (unit GPa) in the Transversely Isotropic material due to source actuating along 1-direction. a) σ_{11} b) σ_{22} c) σ_{33} d) σ_{32} or σ_{23} e) σ_{31} or σ_{13} f) σ_{21} or σ_{12}

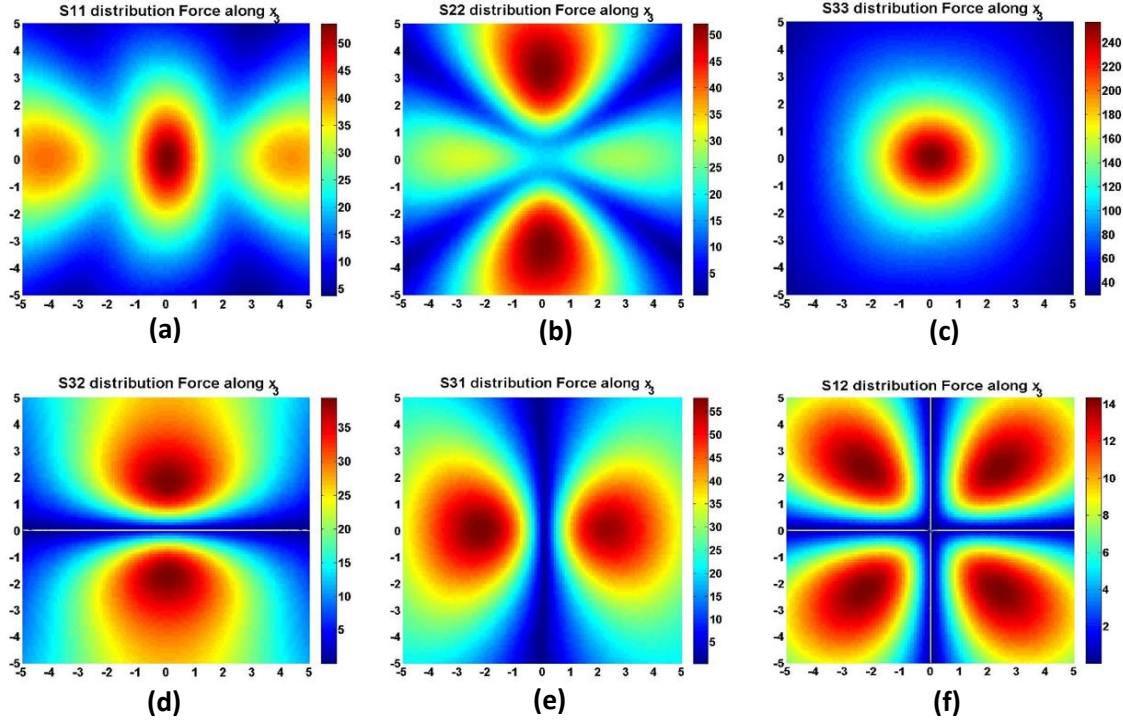


Fig. 5.8. Numerical computation of Stress Green's function (unit GPa) in the Transversely Isotropic material due to source actuating along 3-direction. a) σ_{11} b) σ_{22} c) σ_{33} d) σ_{32} or σ_{23} e) σ_{31} or σ_{13} f) σ_{21} or σ_{12}

CHAPTER 6

NUMERICAL COMPUTATION OF WAVE FIELD WITH THE IMPLEMENTATION OF DPSM

For numerically computing the wave field in anisotropic media, we institute the analytical model developed for the Green's function into a numerical technique called Distributed point source method (DPSM). Therefore, we first provide a brief introduction to DPSM. DPSM is a recently developed mesh-free semi-analytical technique developed by Placko and Kundu (Placko and Kundu 2001, Placko, Kundu et al. 2002). They used the technique to model the wave propagation in fluid media, and the technique was further developed by Banerjee (Banerjee and Kundu 2007) to model the isotropic solids. DPSM is used because it helps to overcome the limitations such as the inability to correctly model critical reflection phenomena, failure to adapt to the change in the interface curvature and necessity of far-field approximation. In DPSM, the Green's function is essential to calculate the displacement and stress profile and simulate the wave propagation behavior.

DPSM, as the name suggests, is the numerical technique based on distributing the source and target points in the actuator such as transducer and boundary and interfaces of the problem geometry. The ultrasonic field generated by the source such as transducer is the summation of the field generated due to all the point sources distributed at the transducer. Similarly, at the interface, there are transmitted and reflected field which is represented by placing the two layers of point sources on either side of the interface. Then, the source strengths of the point sources distributed over the transducer and the interface

is calculated by satisfying the boundary and the interface continuity conditions as required. Finally, displacement and stress profile in the anisotropic medium and the pressure profile in the fluid medium can be calculated with the help of the source strengths.

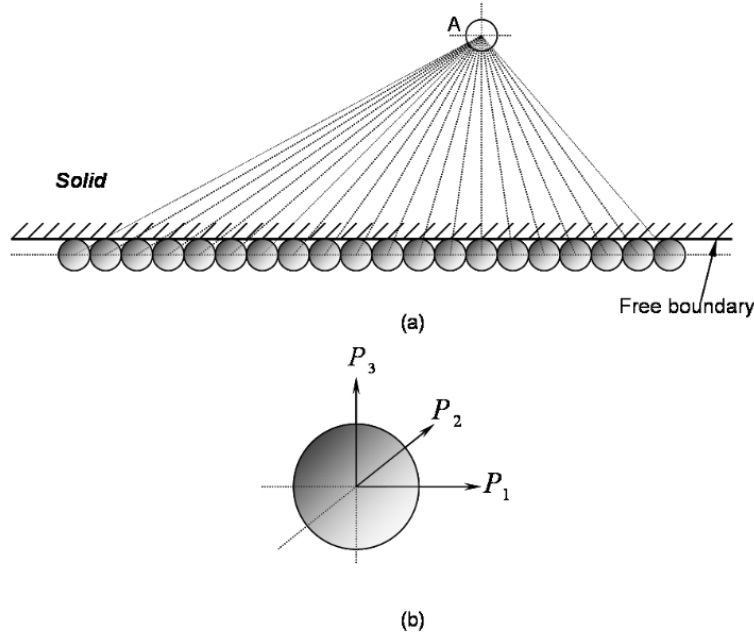


Fig. 6.1. a) the total field at A is calculated by superposing the contribution of all point sources distributed along the boundary of the anisotropic medium. b) the three mutually perpendicular forces that are contained in the point source.

6.1 Numerical Computation of Wavefield in Anisotropic Half-space

Now that we are acquainted with the theory of DPSM, we will compute the ultrasonic wave field in anisotropic half space. The schematic diagram (Fig 6.2) illustrates the setup that has been used for the numerical simulation using DPSM. A circular transducer and an anisotropic half-space are immersed in the fluid. The point sources are distributed below the transducer and on both sides of the interface between the two media. The contribution of different point sources is as shown by the lines connecting the relevant

point sources to the points of interest (C, D). The total ultrasonic field at any arbitrary point C in the anisotropic solid is produced by the superposition of the strength of all the point sources denoted by A_{I*} whereas the total ultrasonic field at any arbitrary point D in the fluid is produced by the superposition of the strength of all the point sources denoted by A_s and A_I . However, at the moment those source strengths required are unknown. Pertaining to the modeling of the current problem, the length of the interface is taken to be 10mm and 115 point sources were distributed on either side of the interface following the wave length - source diameter rule explicitly described in the previous articles (Banerjee 2007, Banerjee and Kundu 2007). A 1 MHz transducer with the diameter of 2 mm is submerged in to the water and 100 point sources were distributed concentrically just below its transmitting face. The distance between the transducer and interface is taken as 5 mm. For the actuation of transducer, unit velocity is prescribed on the transducer face.

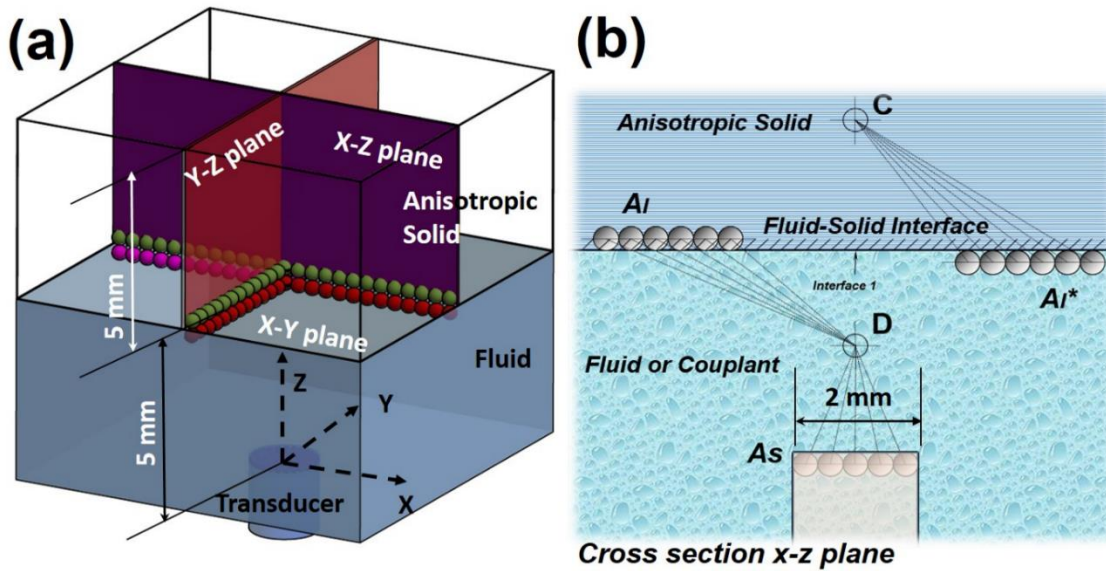


Fig. 6.2 a) Schematics (not to scale) of the wave field computation problem in anisotropic solid half space, point sources distributed over the x-y plane, however, only two orthogonal line of point sources are shown b) cross-section view of the NDE problem along x-z plane.

First, to calculate the unknown source strengths, we need to solve the satisfied boundary conditions (Banerjee 2007, Banerjee and Kundu 2007). If we assume the normal velocity at the transducer face to be V_{s0} , the boundary condition on the transducer surface can be written as

$$M_{SS}A_S + M_{SI}A_I = V_{s0} \quad (31)$$

The displacement normal at the fluid-anisotropic interface should be continuous.

$$DF3_{IS}A_S + DF3_{II}A_I = DS3_{II^*}A_I^* \quad (32)$$

Also, the normal compressive stress in the anisotropic and pressure in the fluid should be continuous at the interface.

$$Q_{IS}A_S + Q_{II}A_I = -S33_{II^*}A_I^* \quad (33)$$

The shear stresses in the anisotropic medium should vanish at the interface.

$$\begin{aligned} S31_{II^*}A_I^* &= 0 \\ S32_{II^*}A_I^* &= 0 \end{aligned} \quad (34)$$

Where, \mathbf{M} represents the velocity Green's function matrix in the fluid, \mathbf{Q} represents the pressure Green's function matrix in the fluid, $\mathbf{S33}$, $\mathbf{S31}$ and $\mathbf{S32}$ represents the stress Green's function matrix in the anisotropic material for σ_{33} , σ_{31} and σ_{32} , respectively. $\mathbf{DF3}$ is the displacement Green's function matrix in the fluid in the x_3 direction, $\mathbf{u3}$ is the displacement Green's function in the solid in the x_3 direction. SS means the wave field on the surface S due to the source layer S , similarly II^* means the respective wave field at the

interface I due to the source layer I^* . By solving the equations (31), (32), (33), (34) as shown in matrix form (Banerjee and Kundu 2007, Banerjee, Kundu et al. 2007) below, we can calculate the source strengths.

$$\begin{bmatrix} M_{SS} & M_{SI} & 0 \\ Q_{IS} & Q_{II} & S33_{II^*} \\ DF3_{IS} & DF3_{II} & -DS3_{II^*} \\ 0 & 0 & S31_{II^*} \\ 0 & 0 & S32_{II^*} \end{bmatrix} \begin{Bmatrix} A_S \\ A_I \\ A_I^* \end{Bmatrix} = \begin{Bmatrix} V_{S0} \\ 0 \\ 0 \end{Bmatrix} \quad (35)$$

From the matrix equation Eq. 35, we can see that to implement the standard procedure of DPSM (Banerjee 2007, Banerjee and Kundu 2007), the Green's function for both the fluid and the solid media needs to be computed.

Hence, the Green's function terminologies required needed for the formulation of DPSM is put together for the convenience and computation of wave field in the respective domains.

6.1.1 Expressions for Velocity, Pressure and Displacement Green's Function in fluid

Let's assume the fluid to be a homogeneous isotropic medium that has no shear strength and equal pressure in all direction. The Green's Function terminologies (Banerjee 2007, Banerjee and Kundu 2007) at any target point, \mathbf{x} due to source acting at \mathbf{y} can be expressed as follows.

$$M = \begin{bmatrix} f(x_{t1}^1, r_1^1) & f(x_{t1}^2, r_1^2) & \dots & f(x_{t1}^{N-1}, r_1^{N-1}) & f(x_{t1}^N, r_1^N) \\ f(x_{t2}^1, r_2^1) & f(x_{t2}^2, r_2^2) & \dots & f(x_{t2}^{N-1}, r_2^{N-1}) & f(x_{t2}^N, r_2^N) \\ f(x_{t3}^1, r_3^1) & f(x_{t3}^2, r_3^2) & \dots & f(x_{t3}^{N-1}, r_3^{N-1}) & f(x_{t3}^N, r_3^N) \\ \dots & \dots & \dots & \dots & \dots \\ f(x_{tM}^1, r_M^1) & f(x_{tM}^2, r_M^2) & \dots & f(x_{tM}^{N-1}, r_M^{N-1}) & f(x_{tM}^N, r_M^N) \end{bmatrix}_{MXN}$$

Where, $f(x_m^m, r_n^m) = \frac{x_m^m \exp(ik_f r_n^m)}{i\omega\rho(r_n^m)^2} (ik_f - \frac{1}{r_n^m})$

$$Q = \begin{bmatrix} \frac{\exp(ik_f r_1^1)}{r_1^1} & \frac{\exp(ik_f r_1^2)}{r_1^1} & \dots & \dots & \frac{\exp(ik_f r_1^M)}{r_1^1} \\ \frac{\exp(ik_f r_2^1)}{r_2^1} & \frac{\exp(ik_f r_2^2)}{r_2^1} & \dots & \dots & \frac{\exp(ik_f r_2^M)}{r_2^1} \\ \dots & \dots & \dots & \dots & \dots \\ \dots & \dots & \dots & \dots & \dots \\ \frac{\exp(ik_f r_N^1)}{r_N^1} & \frac{\exp(ik_f r_N^2)}{r_N^1} & \dots & \dots & \frac{\exp(ik_f r_N^M)}{r_N^1} \end{bmatrix}_{NXM}$$

$$DFt = \begin{bmatrix} g(R_{t1}^1, r_1^1) & g(R_{t1}^2, r_1^2) & \dots & g(R_{t1}^{N-1}, r_1^{N-1}) & g(R_{t1}^N, r_1^N) \\ g(R_{t2}^1, r_2^1) & g(R_{t2}^2, r_2^2) & \dots & g(R_{t2}^{N-1}, r_2^{N-1}) & g(R_{t2}^N, r_2^N) \\ g(R_{t3}^1, r_3^1) & g(R_{t3}^2, r_3^2) & \dots & g(R_{t3}^{N-1}, r_3^{N-1}) & g(R_{t3}^N, r_3^N) \\ \dots & \dots & \dots & \dots & \dots \\ g(R_{tN}^1, r_N^1) & g(R_{tN}^2, r_N^2) & \dots & g(R_{tN}^{N-1}, r_N^{N-1}) & g(R_{tN}^N, r_N^N) \end{bmatrix}_{NXM}$$

Where $g(R_{in}^m, r_n^m) = \frac{1}{\rho\omega^2} \left[\frac{1}{r} ik_f R_{in}^m e^{ik_f r_n^m} - \frac{e^{ik_f r_n^m}}{(r_n^m)^2} R_{in}^m \right]; R_{in}^m = \frac{x_{in}^m - y_{in}^m}{r_{in}^m}; t, i = 1, 2, 3$

6.1.2 Expressions for Displacement and Stress Green's Function in Anisotropic Solid

The Green's Function terminologies for the anisotropic solid are formulated with the help of the expressions developed in the previous chapter 3. The equation used is

displacement Green's Function eq. 28 and stress Green's Function eq. 30 which are written below.

$$g_{mp}(x_n, \omega) = \frac{i\omega f_p}{2(2\pi)^2 \rho} \sum_{z=1}^3 \int_{r=0}^{r=1} \int_{\theta=0}^{\theta=\pi} \int_{\phi=0}^{\phi=2\pi} \left[(s_z)^3 (P_{mp})^{(z)} \exp(i(k_i x_i)^{(z)}) \sin\theta d\theta d\phi \right] \\ + \frac{1}{2(2\pi)^2 \rho |x|} \int_0^{2\pi} (s_z)^2 (P_{mp})^{(z)} d\phi \quad (28)$$

$$\varepsilon^p_{mj} = \frac{1}{2} (u^p_{m,j} + u^p_{j,m}) \quad (29)$$

$$\sigma^p_{ik}(\mathbf{x}) = C_{ikmj} \varepsilon^p_{mj}(\mathbf{x}) \quad (30)$$

$$DS3 = \begin{bmatrix} g_3^{1_1} & g_3^{2_1} & \dots & \dots & g_3^{M_1} \\ g_3^{1_2} & g_3^{2_2} & \dots & \dots & g_3^{M_2} \\ \dots & \dots & \dots & \dots & \dots \\ \dots & \dots & \dots & \dots & \dots \\ g_3^{1_N} & g_3^{2_N} & \dots & \dots & g_3^{M_N} \end{bmatrix}_{NX3M} \quad \text{where, } g_3^{m_n} = [g_{31}^m \quad g_{32}^m \quad g_{33}^m]_n$$

$$S3i = \begin{bmatrix} s_{3i}^{1_1} & s_{3i}^{2_1} & \dots & \dots & s_{3i}^{M_1} \\ s_{3i}^{1_2} & s_{3i}^{2_2} & \dots & \dots & s_{3i}^{M_2} \\ \dots & \dots & \dots & \dots & \dots \\ \dots & \dots & \dots & \dots & \dots \\ s_{3i}^{1_N} & s_{3i}^{2_N} & \dots & \dots & s_{3i}^{M_N} \end{bmatrix}_{NX3M} \quad \text{where, } s_{3i}^{m_n} = [\sigma_{3i}^m \quad \sigma_{3i}^m \quad \sigma_{3i}^m]_n \text{ and } i=1,2,3$$

By substituting the Green's function terminologies as required in the matrix equation Eq. 35, we can now calculate the source strengths. The source strengths are obtained hence known for each layer by solving the simple linear algebra problem put forth by the matrix equation Eq. 35.

After obtaining the source strengths, we can now compute the wave field for the anisotropic half space media. As we have mentioned before, we compute the wave field for three different types of anisotropic material: a) Transversely isotropic, b) Fully orthotropic, c) Monoclinic material.

6.2 Processes to Speed up the Computation

6.2.1 Sequential Mapping of Poly-Crepitus Green's Function

In accordance to DPSM, the ultrasonic field generated at any arbitrary target point is the summation of the field generated due to all the point sources distributed at the transducer for which the Green's function needs to be computed. Furthermore, looking at the derived Green's function expression, we have realized that to calculate the Green's function, we need to consider the waves are propagating in all possible direction which is accomplished by integrating over the sphere and summing all three wave modes. However, after implementing the Green's function expression, it has been realized that the calculation of Green's function due to multiple source points is computationally demanding and inefficient such that it is virtually impossible to compute the full wave field in the anisotropic media in a time efficient manner even for a simple half-space problem. Therefore, to get rid of computational strain and the time inefficiency, we introduced a method called Sequential mapping of Green's function. It followed a simple yet brilliant argument that the Green's function at a target point is always same due to a unit load acting on the source point. That is to say, the Green's function at a target point due to a source is always constant, given the direction cosine of the line joining the source-target combination is constant.

Based on this argument, further, the following method is implemented in the code. Let's assume a set of n number of source points as well as m number of target points in a 2D system as shown in Fig 6.3. Now to implement the sequential mapping of Green's function, the number of target points is extended from m to $(2m-1)$ as shown in Fig 6.3(a) and (b). The Green's function at $(2m-1)$ extended target points due to a central point source is calculated only once as shown in Fig 6.3(c). Then the Green's function at m original target points is sequentially mapped and appropriately assigned by mimicking the central point source located at the location of the point sources below the actuation plane. For illustration, the allocation of $(2m-1)$ Green's function to the original m target point due to the first source point is shown in Fig 6.3(d). In case of first source point, the Green's function from m -th to $(2m-1)$ -th is allocated to the original target points as illustrated in Fig 6.3(d). Due to this technique, the process with 'conventional DPSM,' which originally demanded $(m*n)$ computations of Green's function is reduced to only $(2m-1)$ computations and hence reduced the computation time by the factor of $((2m-1) / m*n)$. Similarly, the mapping technique is implemented in 3D. In case of a 3D system, the number of target points is extended from m_1*m_2 to $(2m_1-1) * (2m_2-1)$ as shown in Fig 6.3(e) and (f). It can be seen that the Green's function at the target point (blue box) due to central source point is same as the Green's function at the target point (yellow box) due to corner source point as shown in Fig 6.3(f). Now the Green's function at the $(2m_1-1) * (2m_2-1)$ extended target points due to the central point source is calculated. Then the $(2m_1-1) * (2m_2-1)$ Green's function is sequentially mapped to the original set of target points due to all n_1*n_2 number of point sources in a similar manner described for the 2D system. For 3D system, the computation time is reduced by the factor of $(2m_1-1) * (2m_2-1) / (m_1*m_2) * (n_1*n_2)$.

Please visit the code named Aniso_green.m in the appendix for the detailed implementation and understanding of the technique.

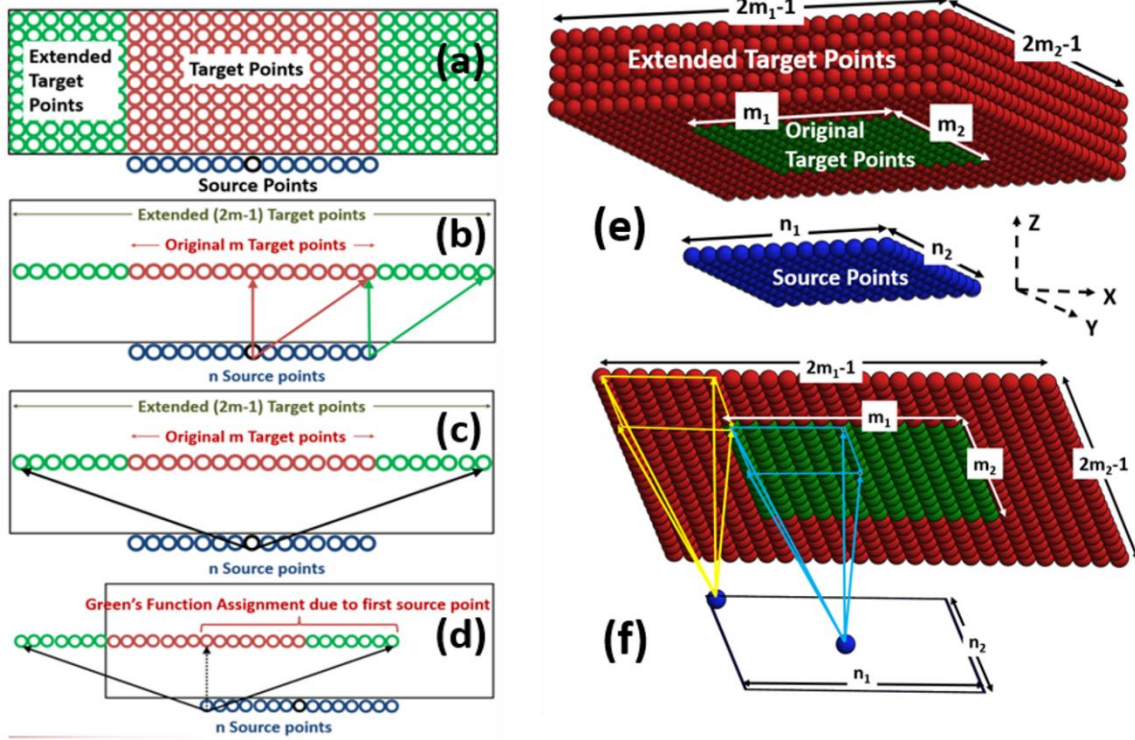


Fig. 6.3: A schematics showing the sequential mapping of Green's function, a) source and target point combinations b) extended target points in 2D c) Calculated Green's function on extended point sources d) Assignment of Green's function for an edge source e) source-target combinations in 3D, f) sequential mapping of 3D Green's function.

6.2.2 Maximizing the Discretization Angle for Anisotropic Green's function

Eq. 28 and 30 are computed numerically. The integral requires an optimized discretization angle that can result converged Green's function while reducing the computational time.

Average of resultant absolute displacement were computed with different degrees of discretization along θ and ϕ in transversely isotropic, orthotropic and monoclinic material (please refer section 7 for material properties) along with a line at a distance of 1mm from a point source at 1 MHz frequency. Results with both discretization angles, $\Delta\theta$ and $\Delta\phi$ with

and 0.5° and 1° were almost identical with 0.0001% error in all material class. The average percentage error was calculated for various discretization angles, and the convergence curve is shown in Fig. 6.4a. Computation burden with ten as the discretization angle is still comparatively massive and unacceptable. However, it can be seen that the discretization angle between 3° and 5° resulted almost converged result with error $< \sim 1.3\%$, but the computational burden was reduced significantly. Hence, for the proposed virtual NDE experiment at 1 MHz, an optimized 5° discretization is used considering the tradeoff and benefit between the accuracy and the computational efficiency. Standardizing the discretization angle is valuable for universal application of DPSM. Further the overall gain was estimated with the computational efficiency, after implementing both the sequential mapping and an optimized discretization angle for the problem described above in Fig. 6.2, took only 1.6 hours. Fig. 6.4b shows, how two additional improvements reduced the computational burden of DPSM unprecedentedly by ~ 90 times compared to the conventional DPSM with ten as the discretization angle. A standard computer with Intel(R) Core(TM) i7-6500U CPU @ 2.5 GHz with 8 GB RAM was used.

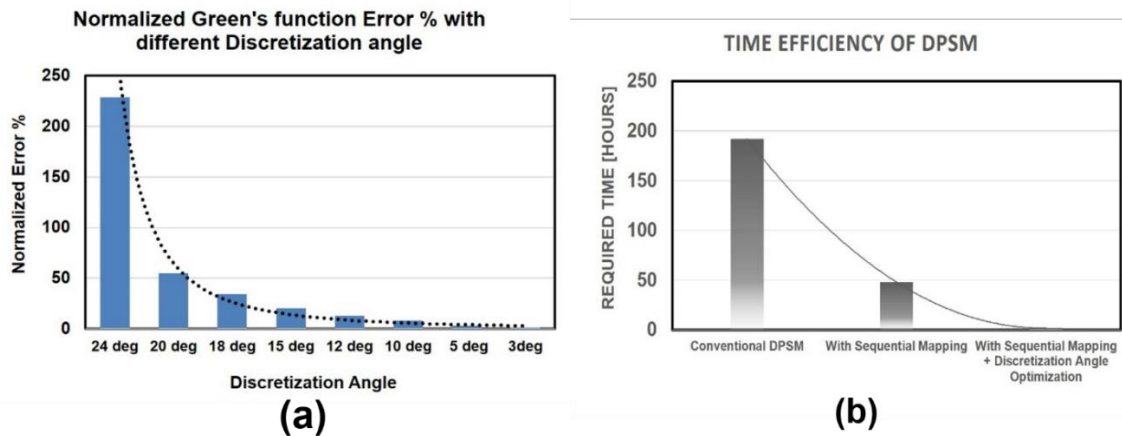


Fig. 6.4: a) Convergence study with the discretization angle for Green's function computation b) Increase in computational efficiency while solving a virtual NDE problem described in Fig. 6.2 in a transversely isotropic medium.

6.3 Wavefield Modeling of Transversely Isotropic Half-space

We first compute the wave field for the transversely isotropic half-space. While doing so, we first confirm that the source strengths are appropriately computed by solving the governing matrix eq. 35. To do so, we calculate both the pressure and normal stresses at the fluid-solid interface to check if the boundary conditions are matched (Fig. 6.5). The verification was performed by applying the convergence criteria ($r \leq \lambda/2\pi$) where the distance between two adjacent point sources was $2r$, discussed in previous publications (Banerjee and Kundu 2007).

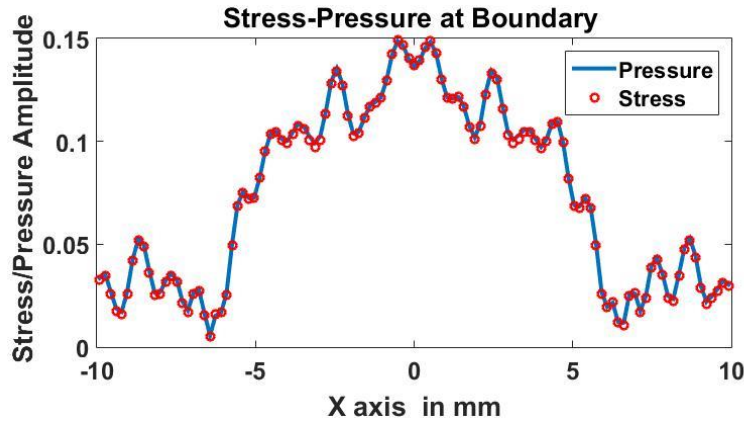


Fig 6.5. Pressure and normal stress (σ_{33}) distribution at the fluid-solid interface

Now that, the matching of the boundary condition at the fluid-solid interface is confirmed, we proceed to compute the wave field for the full domain, i.e., pressure in fluid and the stress in solid. First, we compute the stresses (σ_{11} and σ_{33}) and pressure for the full domain which is shown in fig 6.6a and b respectively. We compare the solution with the wave stresses field in isotropic half space (fig 6.7a and b) so that we can physically understand

the wave phenomena in transversely isotropic material and differentiate it in comparison to the isotropic material.

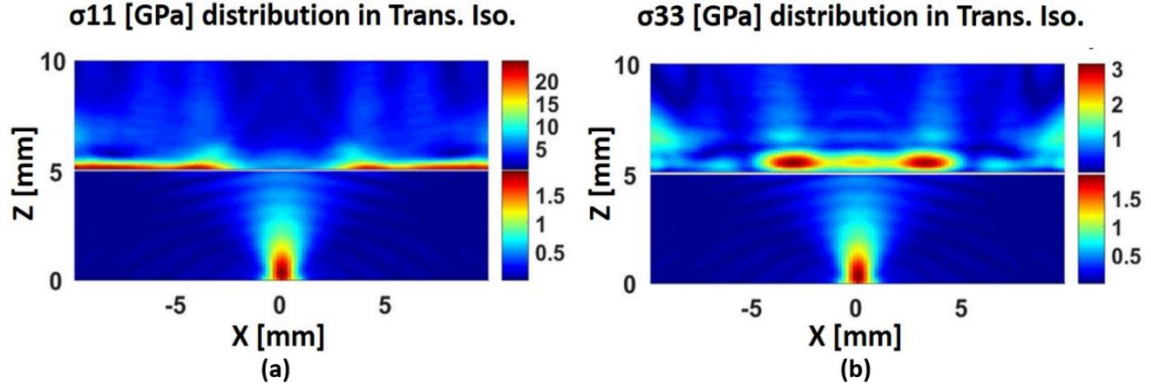


Fig 6.6. a) Stress11 (σ_{11}) distribution in transversely isotropic half-space b) Stress33 (σ_{33}) distribution in transversely isotropic half-space in GPa

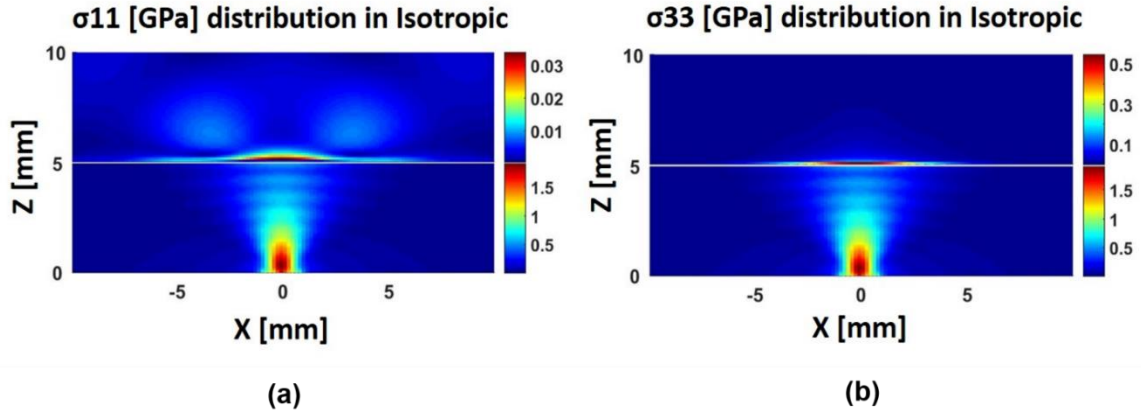


Fig 6.7. a) Stress11 (σ_{11}) distribution in isotropic half-space b) Stress33 (σ_{33}) distribution in isotropic half space in GPa

For the comparison of the stress fields in transversely isotropic and isotropic material, we assume the transversely isotropic material as a unidirectional composite material with fiber direction along the x-axis such that the y-z plane is the plane of isotropy. We can see that the maximum or dominant wave energy is bifurcating along the fiber direction for both stress field as shown in fig 6.6a and b which is in agreement with our theoretical understanding. Conversely, in case of isotropic material we see that the

maximum or dominant wave energy is propagating along the along the actuation direction for both stress field as shown in fig 6.7a and b.

We now have successfully computed the wavefield in a transversely isotropic material exhibiting the correct physics of wave phenomena. We also compute the wave field in the orthotropic and monoclinic material. The wavefield in x-z and y-z planes were computed, such that the difference in wave fields are made apparent in oppose to isotropic material which exhibits same wave field on both x-z and y-z planes.

6.4 Wavefield Modeling of Orthotropic Half-space

The stress fields in the orthotropic material on the x-z plane (Fig 6.8 a & b) and y-z planes (Fig 6.9 a & b) are presented.

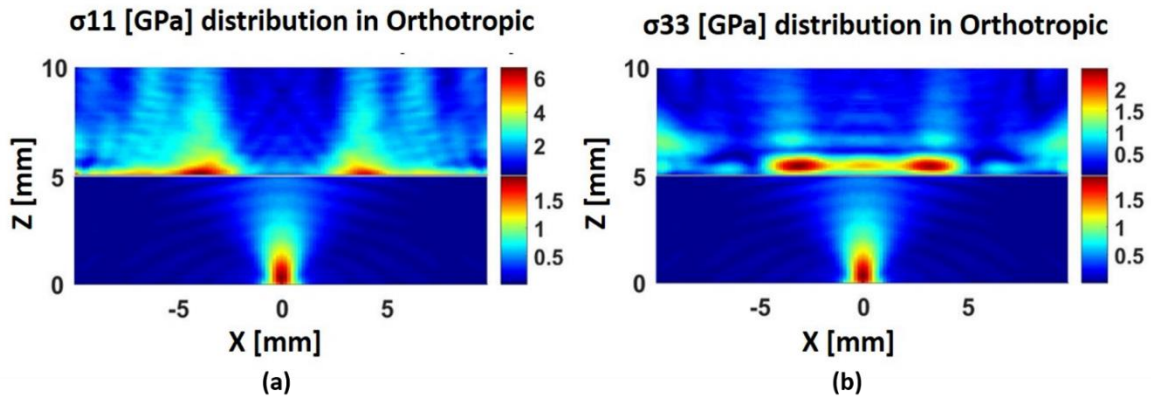


Fig 6.8. Wave field plot on x-z plane a) Stress11 (σ_{11}) distribution in fully orthotropic half-space b) Stress33 (σ_{33}) distribution in fully orthotropic half space

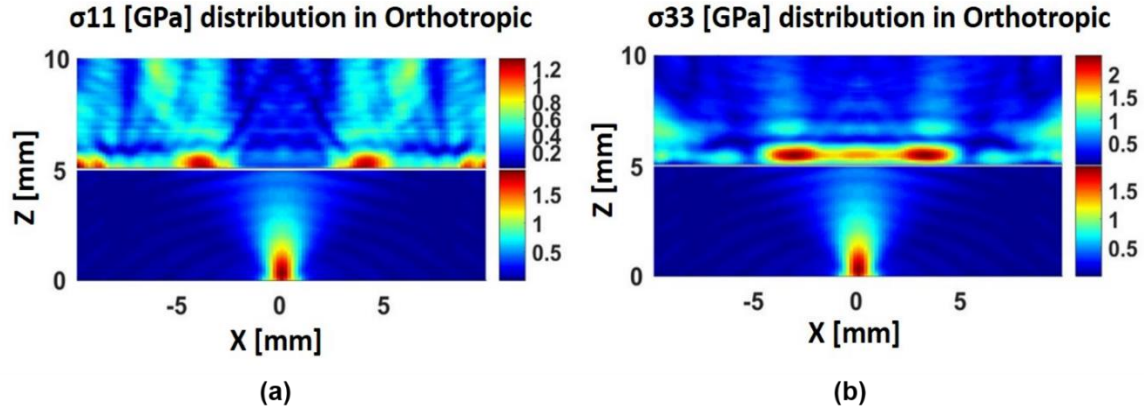


Fig 6.9. Wave field plot on y-z plane a) Stress11 (σ_{11}) distribution in fully orthotropic half-space b) Stress33 (σ_{33}) distribution in fully orthotropic half space

6.5 Wavefield Modeling of Monoclinic Half-space

The stress fields in the orthotropic material on the x-z plane (Fig 6.10 a & b) and y-z planes (Fig 6.11 a & b) are presented.

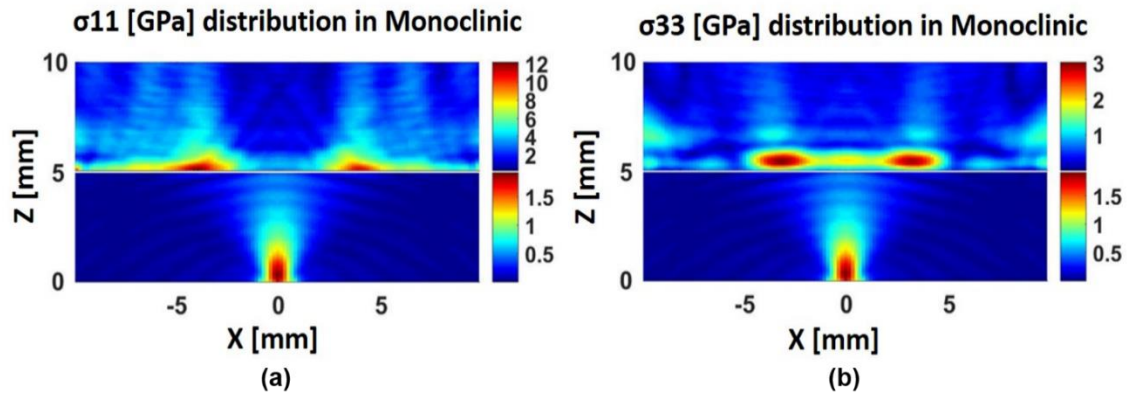


Fig 6.10. Wave field plot on x-z plane a) Stress11 (σ_{11}) distribution in monoclinic half space b) Stress33 (σ_{33}) distribution in monoclinic half space

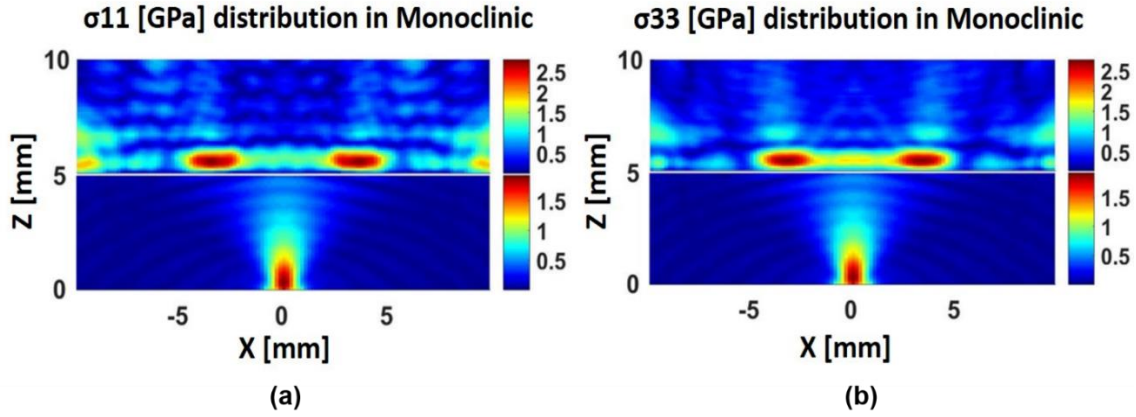


Fig 6.11. Wave field plot on y-z plane a) Stress11 (σ_{11}) distribution in monoclinic half space b) Stress33 (σ_{33}) distribution in monoclinic half space

The stress fields in fully orthotropic and monoclinic materials on x-z and y-z planes are compared. The qualitative and quantitative differences are evident. The differences could be explained by the modal slowness behavior shown by the wave mode on the x-z plane for all the three materials plotted in Fig 4.5, 4.6, & 4.7. The maximum wave energy on an x-z plane is contributed mostly by the quasi-longitudinal wave mode and minimally influenced by the other quasi-shear modes, hence to the qualitative similarities of the wave fields between the orthotropic and monoclinic material over the x-z plane are evident. Similarly, the qualitative differences of the wave fields between the orthotropic and monoclinic material over the y-z plane are evident from the modal slowness behavior shown by the wave mode on the y-z plane for all the three materials.

CHAPTER 7

CONCLUSION AND FUTURE ENDEAVORS

Understanding the wave propagation behavior is a crucial step. Consequently, it helps in the understanding of the physics of different materials and critically comprehend the differences between them. First, the fundamental conceptions of wave propagation behavior in the anisotropic material have been discussed. The modal waves have been visualized by solving the Christoffel's Equation. By incorporating those notions, the anisotropic Green's displacement and stress function have been developed, first using quadruple Fourier transformation for the physical understanding then again using a novel method known as Radon transform and Spectral Resolution Theorem in the spherical coordinate system for the more straightforward implementation into the MATLAB code. Finally, wave propagation behavior has been simulated and modeled for the different anisotropic medium by numerical computing the Green's function and employing it into Distributed point source method (DPSM). DPSM technique has been used in modeling the ultrasonic field generated by a finite size transducer near a fluid-solid interface, and the field is computed inside both fluid and solid media. A method named Sequential Mapping of Poly-Crepitus Green's Function has been introduced for the time-efficient computation of the wave field. In conclusion, in this thesis work, we were able to successfully model the full wave field in an accurate and time efficient manner.

For the future endeavors, this technique will further be used for the computational anisotropic wavefield modeling in a more complex geometry and anisotropy which will

ultimately assist in the advancement of NDE community. Shortly, this technique will be used in computing the wave field in structures such as composite plates, multilayered media, and porous media.

REFERENCES

Achenbach, J. (1975). Wave propagation in elastic solids. Amsterdam, Elsevier Science Publishers B. V.

Auld, B. A. (1990). Acoustic Fields and Waves in Solids, Wiley.

B. P. Newberry, R. B. T. (1989). "A Paraxial Theory for the Propagation of Ultrasonic Beams in Anisotropic Solids." Journal of the Acoustical Society of America **85**: 2290.

Ballisti, C. H. (1983). "The multiple multipole method (MMP) in electro and magnetostatic problems." IEEE Transactions on Magnetics **19**(6): 2367.

Banerjee, S., Alnuaimi, N., Kundu, T. (2007). "DPSM Technique for Ultrasonic Field Modelling Near Fluid-Solid Interface." Ultrasonics **46**(3): 235-250.

Banerjee, S., Das, S., Kundu, T., Placko, D. (2009). "Controlled Space Radiation concept for mesh-free semi-analytical technique to model wave fields in complex geometries." Ultrasonics **48**(8): 615-622.

Banerjee, S. and T. Kundu (2006). "Elastic wave propagation in sinusoidally corrugated waveguides." Journal of the Acoustical Society of America **119**(4): 2006-2017.

Banerjee, S. and T. Kundu (2007). Advanced Application of Distributed Point Source Method - Ultrasonic Field Modeling in Solid media. DPSM for Modeling Engineering Problems. T. Kundu and D. Placko. Hoboken, New Jersey, USA, John & Willey Publication.

Banerjee, S. and T. Kundu (2007). "Advanced applications of distributed point source method-ultrasonic field modeling in solid media." DPSM for Modeling Engineering Problems: 143-229.

Banerjee, S., et al. (2007). "DPSM technique for ultrasonic field modelling near fluid–solid interface." Ultrasonics **46**(3): 235-250.

Banerjee, S., Kundu, T. (2006). "Symmetric and Anti-symmetric Rayleigh-Lamb modes in Sinusoidally corrugated waveguides: An Analytical approach." International Journal of Solids and Structures **43**(6551-6567).

Banerjee, S., Kundu, T. (2007). "Ultrasonic Field Modeling in Plates Immersed in Fluids." International Journal of Solids and Structures **44**(18-19): 6013-6029.

Banerjee, S., Kundu, T. (2008). "Elastic Wave Field Computation in Multilayered Non-Planar Solid Structures: A Mesh-free Semi-Analytical Approach." Journal of Acoustical Society of America **123**(3): 1371-1382.

Banerjee, S., Kundu, T. (2008). "Semi-Analytical Modeling of Ultrasonic Fields in Solids with Internal Anomalies Immersed in a Fluid." Wave Motion **45**(5): 581-595.

Biondi, B. (1992). "Solving the frequency-dependent Eikonal equation." 62nd Ann. Internat. Mtg., Soc. Expl. Geophys. Expanded Abstracts: 1351.

Burridge, R. (1971). "Lamb's problem for an anisotropic half-space." The Quarterly Journal of Mechanics and Applied Mathematics **24**(1): 81-98.

C. Rajamohan, J. Raamachandran (1999). "Bending of anisotropic plates by charge simulation method." Advances in Engineering Software **30**(5): 369.

Cara A.C. Leckey, M. D. R., F. Raymond Parker (2014). "Guided waves in anisotropic and quasi-isotropic aerospace composites: Three-dimensional simulation and experiment." Ultrasonics **54**: 385-394.

Carcione, J. M. (2007). Wave fields in real media: Wave propagation in anisotropic, anelastic, porous and electromagnetic media, Elsevier.

Christoffel, E. (1877). "Ueber die Fortpflanzung von Stößen durch elastische fest Körper." Annali di Matematica **8**: 193:243.

Deans, S. R. (2007). The Radon transform and some of its applications, Courier Corporation.

Every, A. G. and K. Y. Kim (1996). "Determination of elastic constants of anisotropic solids from elastodynamic Green's functions." Ultrasonics **34**(2–5): 471-472.

Every, A. G., et al. (2004). "Phonon Focusing Caustics in Crystals and their Diffraction Broadening at Ultrasonic Frequencies." Trans. Roy. Soc. of South Africa **58**(2).

Giurgiutiu, V. (2014). Structural Health Monitoring with Piezoelectric Wafer Active Sensors, 2nd Ed., Elsevier Academic Press.

Hafner, C. (1985). "MMP calculations of guided waves." IEEE Transactions on Magnetics **21**: 2310.

Handbook, D. o. D. (2009 April 7). NONDESTRUCTIVE EVALUATION SYSTEM RELIABILITY ASSESSMENT: Ultrasonic Test System. Appendix C, Department of Defense. **MIL-HDBK-1823A**.

Hood, J. A. and R. B. Mignogna (1995). "Determination of elastic moduli in anisotropic media from ultrasonic contact measurements." Ultrasonics **33**(1): 45-54.

Imhof, M. G. (2004). "Computing the elastic scattering from inclusions using the multiple multipoles method in three dimensions." Geophysics, J. Int. **156**: 287.

J, B. M. S.-S. F. (2007). Boundary Integral Equations and Boundary Elements Methods in Elastodynamics. Advances in wave propagation in heterogeneous earth, Advances in Geophysics. V. M. R. D. R-S Wu. New York, Boston, Elsevier-Academic Press, . **48**.

J Moll, C. R.-S., R T Schulte, T Klinkert, C -P Fritzen, A Kolb (2011). "Modelling of Wave-Based SHM Systems Using the Spectral Element Method, under Interactive Simulation and Visualization of Lamb Wave Propagation in Isotropic and Anisotropic Structures." Journal of Physics: Conference Series **305**: 012095.

J. J. Wen, M. A. B. (1988). "A Diffraction Beam Field Expressed as the Superposition of Gaussian Beams." Journal of the Acoustical Society of America **83**: 1752.

Kim, K. Y., et al. (1994). "Focusing of fast transverse modes in (001) silicon at ultrasonic frequencies." Journal of Acoustical Society of America **95**(4): 1942.

Kraut, E. A. (1963). "Advances in the theory of anisotropic elastic wave propagation." Reviews of Geophysics **1**(3): 401-448.

Lane, C. (2014). Wave Propagation in Anisotropic Media. The Development of a 2D Ultrasonic Array Inspection for Single Crystal Turbine Blades, Springer: 13-39.

Li, B., et al. (2013). "Damage localization in composite laminates based on a quantitative expression of anisotropic wavefront." Smart Materials and Structures **22**(6): 065005.

M, S.-S. F. J. C. (1991). "Diffraction of P, SV and Rayleigh waves by topographic features: a boundary integral formulation." Bull. Seism. Soc. Am. **81**: 2234-2253.

M, S.-S. F. J. C. (1993). "Topographic effects for incident P, SV and Rayleigh waves." Tectonophysics **218**: 113-125.

M., P., et al. (2000). "Angular spectrum approach for the computation of group and phase velocity surfaces of acoustic waves in anisotropic materials." Ultrasonics **38**: 232-236.

Mal, A. K., et al. (1991). "Ultrasonic nondestructive evaluation of cracked composite laminates." Composites Engineering **1**(2): 85-101.

Marguères, P. and F. Meraghni (2013). "Damage induced anisotropy and stiffness reduction evaluation in composite materials using ultrasonic wave transmission." Composites Part A: Applied Science and Manufacturing **45**(0): 134-144.

Moser, B., et al. (2005). "Damage accumulation during cyclic loading of a continuous alumina fibre reinforced aluminium composite." Scripta Materialia **53**(10): 1111-1115.

Mouchtachi, A., et al. (2004). "Ultrasonic Study of Elastic Anisotropy of Material Composite." Applied Composite Materials **11**(6): 341-351.

Nayfeh, A. H. (1995). Wave propagation in layered anisotropic media: With application to composites, Elsevier.

Payton, R. (2012). Elastic wave propagation in transversely isotropic media, Springer Science & Business Media.

Placko, D. and T. Kundu (2001). Theoretical study of magnetic and ultrasonic sensors: dependence of magnetic potential and acoustic pressure on the sensor geometry. Advanced NDE for structural and biological health monitoring. T. Kundu (Ed.), Proceedings of SPIE, SPIE's 6th Annual International Symposium on NDE for Health Monitoring and Diagnostics. Newport Beach, California. **4335**: 52-62.

Placko, D. and T. Kundu (2007). DPSM for modeling engineering problems, John Wiley & Sons.

Placko, D., et al. (2002). Theoretical computation of acoustic pressure generated by ultrasonic sensors in the presence of an interface. Smart NDE and health monitoring of structural and biological systems, SPIE's 7th Annual International Symposium in NDE and Health Monitoring and Diagnostics. San Diego, CA. **4702**: 157-168.

Pointer T, L. E. H. J. A. (1998). "Numerical modeling of seismic waves scattered by hydrofractures: application of the indirect boundary element method." Geophys J., Int. **135**: 289-303.

Pradhan, B., et al. (1999). "Stiffness degradation resulting from 90° ply cracking in angle-ply composite laminates." Composites Science and Technology **59**(10): 1543-1552.

Rahani, E. K., Kundu, T., (2011). "Gaussian-DPSM (G-DPSM) and Element Source Method (ESM) modifications to DPSM for ultrasonic field modeling " Ultrasonics **51**(5): 625-631.

Rokhlin, S. I. C., D. E.; Nagy, P. B. (2011). Physical Ultrasonics of Composites. Oxford, UK, Oxford University Press.

Sachse, W., et al. (1990). "Recent developments in quantitative ultrasonic NDE of composites." Ultrasonics **28**(2): 97-104.

Sahay, S. K., et al. (1992). "Phase and group velocity considerations for dynamic modulus measurement in anisotropic media." Ultrasonics **30**(6): 373-382.

Sharma, M. D. (2002). "Group velocity along general direction in a general anisotropic medium." International Journal of Solids and Structures **39**(12): 3277-3288.

Shaw, R. P. (1979). Ch.6 Boundary Integral Equation Methods Applied to Wave Problems. Developments in Boundary Element Methods - 1. P. K. B. a. R. Butterfield, Appl Sci. Pub.: 121-153.

Sinclair, C. E. (2009). Elastic wave modelling in anisotropic media using the spectral-element method, The University of Adelaide.

Software, P. (2009). Finite Element Analysis of Propagating Elastic Waves, Weilinger Associates Inc. . **Version: 1-j.6**.

Spies, M. (1999). "Transducer Field Modeling in Anisotropic Media by Superposition of Gaussian Base Functions." Journal of the Acoustical Society of America **105**: 633.

Tverdokhlebov, A., Rose, J. (1988). "On Green's function for elastic waves in anisotropic media." Journal of Acoustical Society of America **83**: 844-870.

Wang, C. Y. and J. D. Achenbach (1992). "A new look at 2-D time-domain elastodynamic Green's functions for general anisotropic solids." Wave Motion **16**(4): 389-405.

Wang, C. Y. and J. D. Achenbach (1993). "A new method to obtain 3-D Green's functions for anisotropic solids." Wave Motion **18**(3): 273-289.

Wang, C. Y., Achenbach, J.D. (1994). "Elastodynamic fundamental solutions for anisotropic solids." Geophys. J. Int. **118**: 384-392.

Willis, J. (1991). "Inclusions and cracks in constrained anisotropic media." Modern Theory of Anisotropic Elasticity and Applications. SIAM, Philadelphia: 87-102.

Willis, J. R. (1973). "Self-Similar Problems in Elastodynamics." Philosophical Transactions of the Royal Society of London A: Mathematical, Physical and Engineering Sciences **274**(1240): 435-491.

X. Zhao., J. L. R. (2003). "Boundary Element Modeling for Defect Characterization potential in a wave guide." International Journal of Solids and Structures **40**(11): 2645.

Yeatts, F. R. (1984). "Elastic radiation from a point force in an anisotropic medium." Phys. Rev. B **29**: 1674-1684.

APPENDIX A

ANISOGREEN.M

```
function[DS1ii,DS2ii,DS3ii, S11ii, S22ii, S33ii, S12ii, S31ii, S32ii]=Aniso_green(Sw_IntrFcCoord_Cent,  
CoordCentSourcePt, C, Theta, Phi, CV, FI, NumTestPt, NumSourcePt_Intface_x, NumSourcePt_Intface_y,  
Solid_rho, w, dTheta, dPhi)
```

```
%% Displacement Green's Function
```

```
%% Initialization
```

```
NumSourceTot=NumSourcePt_Intface_x*NumSourcePt_Intface_y;
```

```
% For Final allocation of Displacements and Stresses
```

```
DS1ii = zeros(NumSourceTot,NumSourceTot,3);
```

```
DS2ii = zeros(NumSourceTot,NumSourceTot,3);
```

```
DS3ii = zeros(NumSourceTot,NumSourceTot,3);
```

```
S11ii = zeros(NumSourceTot,NumSourceTot,3);
```

```
S22ii = zeros(NumSourceTot,NumSourceTot,3);
```

```
S33ii = zeros(NumSourceTot,NumSourceTot,3);
```

```
S12ii = zeros(NumSourceTot,NumSourceTot,3);
```

```
S31ii = zeros(NumSourceTot,NumSourceTot,3);
```

```
S32ii = zeros(NumSourceTot,NumSourceTot,3);
```

```
NumTrgGreenExtnd_x=(2*NumSourcePt_Intface_x-1);
```

```
NumTrgGreenExtnd_y=(2*NumSourcePt_Intface_y-1);
```

```
% For Temporary allocation of Displacements and Stresses
```

```
tu1_11 = zeros(NumTrgGreenExtnd_x,NumTrgGreenExtnd_y,3);
```

```
tu2_11 = zeros(NumTrgGreenExtnd_x,NumTrgGreenExtnd_y,3);
```

```
tu3_11 = zeros(NumTrgGreenExtnd_x,NumTrgGreenExtnd_y,3);
```

```
tS11_11 = zeros(NumTrgGreenExtnd_x,NumTrgGreenExtnd_y,3);
```

```
tS22_11 = zeros(NumTrgGreenExtnd_x,NumTrgGreenExtnd_y,3);
```

```
tS33_11 = zeros(NumTrgGreenExtnd_x,NumTrgGreenExtnd_y,3);
```

```
tS12_11 = zeros(NumTrgGreenExtnd_x,NumTrgGreenExtnd_y,3);
```

```
tS31_11 = zeros(NumTrgGreenExtnd_x,NumTrgGreenExtnd_y,3);
```

```
tS32_11 = zeros(NumTrgGreenExtnd_x,NumTrgGreenExtnd_y,3);
```

```
%% Calculation Starts
```

```
CoordCentSourcePt_x=CoordCentSourcePt(1);
```

```
CoordCentSourcePt_y=CoordCentSourcePt(2);
```

```

CoordCentSourcePt_z=CoordCentSourcePt(3);

for h=1:NumTrgGreenExtnd_y
    for i=1:NumTrgGreenExtnd_x          % total no. of target point

        Sw_TrgLoc = i+(h-1)*NumTrgGreenExtnd_x;
        Tr = [(Sw_IntrFcCoord_Cent(1,Sw_TrgLoc)-CoordCentSourcePt_x),
        (Sw_IntrFcCoord_Cent(2,Sw_TrgLoc)-CoordCentSourcePt_y), (Sw_IntrFcCoord_Cent(3,Sw_TrgLoc)-
        CoordCentSourcePt_z)];

        [u1,u2,u3,S11,S22,S33,S23,S13,S12] = solid_green(Tr, C, Theta, Phi, CV, FI, NumTestPt, Solid_rho,
        w, dTheta, dPhi);

        tu1_11(i,h,:) = u1;
        tu2_11(i,h,:) = u2;
        tu3_11(i,h,:) = u3;
        tS11_11(i,h,:) = S11;
        tS22_11(i,h,:) = S22;
        tS33_11(i,h,:) = S33;
        tS12_11(i,h,:) = S12;
        tS31_11(i,h,:) = S13;
        tS32_11(i,h,:) = S23;

    end
end

for indicey=1:NumSourcePt_Intface_y
    for indicex=1:NumSourcePt_Intface_x          %total number of sources

        for dir=1:3          % total no. of target point

            src_pt = indicex+(indicey-1)*NumSourcePt_Intface_x;
            trg_pts = (NumSourcePt_Intface_x+1-indicex):(NumTrgGreenExtnd_x+1-indicex);

            for indiceyp = 1:NumSourcePt_Intface_y

                sw_index_y = NumSourcePt_Intface_y-indicey+indiceyp;
                trg_val = (indiceyp-1)*NumSourcePt_Intface_x+1:(indiceyp)*NumSourcePt_Intface_x;

                DS1ii(trg_val,src_pt,dir) = tu1_11(trg_pts,sw_index_y,dir); % Displacement in mm
                DS2ii(trg_val,src_pt,dir) = tu2_11(trg_pts,sw_index_y,dir); % Displacement in mm
                DS3ii(trg_val,src_pt,dir) = tu3_11(trg_pts,sw_index_y,dir); % Displacement in mm

                S11ii(trg_val,src_pt,dir) = tS11_11(trg_pts,sw_index_y,dir); % Stress in GPa
                S22ii(trg_val,src_pt,dir) = tS22_11(trg_pts,sw_index_y,dir); % Stress in GPa
                S33ii(trg_val,src_pt,dir) = tS33_11(trg_pts,sw_index_y,dir); % Stress in GPa
                S12ii(trg_val,src_pt,dir) = tS12_11(trg_pts,sw_index_y,dir); % Stress in GPa
            end
        end
    end
end

```

```

        S31ii(trg_val,src_pt,dir) = tS31_11(trg_pts,sw_index_y,dir); % Stress in GPa
        S32ii(trg_val,src_pt,dir) = tS32_11(trg_pts,sw_index_y,dir); % Stress in GPa

    end
end
end
end
display('Green displacement and stress calculated')

```